Geosci. Model Dev., 8, 3179–3198, 2015
www.geosci-model-dev.net/8/3179/2015/
doi:10.5194/gmd-8-3179-2015
© Author(s) 2015. CC Attribution 3.0 License.

Geoscientific Model Development
Open Access

Simulation of atmospheric N_2O with GEOS-Chem and its adjoint: evaluation of observational constraints

K. C. Wells[1], D. B. Millet[1], N. Bousserez[2], D. K. Henze[2], S. Chaliyakunnel[1], T. J. Griffis[1], Y. Luan[1], E. J. Dlugokencky[3], R. G. Prinn[4], S. O'Doherty[5], R. F. Weiss[6], G. S. Dutton[3,7], J. W. Elkins[3], P. B. Krummel[8], R. Langenfelds[8], L. P. Steele[8], E. A. Kort[9], S. C. Wofsy[10], and T. Umezawa[11,12]

[1]Department of Soil, Water, and Climate, University of Minnesota, St. Paul, Minnesota, USA
[2]Department of Mechanical Engineering, University of Colorado at Boulder, Boulder, Colorado, USA
[3]Earth System Research Laboratory, NOAA, Boulder, Colorado, USA
[4]Center for Global Change Science, Massachusetts Institute of Technology, Cambridge, Massachusetts, USA
[5]School of Chemistry, University of Bristol, Bristol, UK
[6]Scripps Institute of Oceanography, University of California, San Diego, La Jolla, California, USA
[7]CIRES, University of Colorado, Boulder, Colorado, USA
[8]CSIRO Oceans and Atmosphere Flagship, Aspendale, Victoria, Australia
[9]Department of Atmospheric, Oceanic, and Space Sciences, University of Michigan, Ann Arbor, Michigan, USA
[10]School of Engineering and Applied Science and Department of Earth and Planetary Sciences, Harvard University, Cambridge, Massachusetts, USA
[11]Center for Atmospheric and Oceanic Studies, Tohoku University, Sendai, Japan
[12]Max-Planck Institute for Chemistry, Mainz, Germany

Correspondence to: D. B. Millet (dbm@umn.edu)

Received: 27 May 2015 – Published in Geosci. Model Dev. Discuss.: 8 July 2015
Revised: 14 September 2015 – Accepted: 17 September 2015 – Published: 8 October 2015

Abstract. We describe a new 4D-Var inversion framework for nitrous oxide (N_2O) based on the GEOS-Chem chemical transport model and its adjoint, and apply it in a series of observing system simulation experiments to assess how well N_2O sources and sinks can be constrained by the current global observing network. The employed measurement ensemble includes approximately weekly and quasi-continuous N_2O measurements (hourly averages used) from several long-term monitoring networks, N_2O measurements collected from discrete air samples onboard a commercial aircraft (Civil Aircraft for the Regular Investigation of the atmosphere Based on an Instrument Container; CARIBIC), and quasi-continuous measurements from the airborne HIAPER Pole-to-Pole Observations (HIPPO) campaigns. For a 2-year inversion, we find that the surface and HIPPO observations can accurately resolve a uniform bias in emissions during the first year; CARIBIC data provide a somewhat weaker constraint. Variable emission errors are much more difficult to resolve given the long lifetime of N_2O, and major parts of the world lack significant constraints on the seasonal cycle of fluxes. Current observations can largely correct a global bias in the stratospheric sink of N_2O if emissions are known, but do not provide information on the temporal and spatial distribution of the sink. However, for the more realistic scenario where source and sink are both uncertain, we find that simultaneously optimizing both would require unrealistically small errors in model transport. Regardless, a bias in the magnitude of the N_2O sink would not affect the a posteriori N_2O emissions for the 2-year timescale used here, given realistic initial conditions, due to the timescale required for stratosphere–troposphere exchange (STE). The same does not apply to model errors in the rate of STE itself, which we show exerts a larger influence on the tropospheric burden of N_2O than does the chemical loss rate over short (< 3 year) timescales. We use a stochastic estimate of the inverse Hessian for the inversion to evaluate the spatial resolution of emission constraints provided by the observations, and find that significant, spatially explicit constraints can be achieved

in locations near and immediately upwind of surface measurements and the HIPPO flight tracks; however, these are mostly confined to North America, Europe, and Australia. None of the current observing networks are able to provide significant spatial information on tropical N_2O emissions. There, averaging kernels (describing the sensitivity of the inversion to emissions in each grid square) are highly smeared spatially and extend even to the midlatitudes, so that tropical emissions risk being conflated with those elsewhere. For global inversions, therefore, the current lack of constraints on the tropics also places an important limit on our ability to understand extratropical emissions. Based on the error reduction statistics from the inverse Hessian, we characterize the atmospheric distribution of unconstrained N_2O, and identify regions in and downwind of South America, central Africa, and Southeast Asia where new surface or profile measurements would have the most value for reducing present uncertainty in the global N_2O budget.

1 Introduction

Nitrous oxide (N_2O) is a long-lived greenhouse gas with a global warming potential approximately 300 times that of CO_2 on a 100-year timescale (Forster et al., 2007). It is also a key player in stratospheric chemistry; N_2O emissions weighted by their ozone depletion potential currently outrank those of any other ozone depleting substance (Ravishankara et al., 2009). N_2O is produced via microbial nitrification and denitrification in soils (Firestone and Davidson, 1989) and ocean waters (Elkins et al., 1978; Cohen and Gordon, 1979; Law and Owens, 1990), with soils contributing the majority of the global flux (Mosier et al., 1998). Agricultural activities such as fertilizer application and animal waste management increase the substrate available for nitrification and denitrification pathways (Maggiotto et al., 2000), leading to enhanced direct on-site emissions as well as indirect emissions downstream due to leaching and runoff (IPCC, 2006). Energy production and transportation (Denman et al., 2007) and biomass burning emissions (van der Werf et al., 2010) also contribute to the global N_2O source. N_2O is lost in the stratosphere via photolysis and reaction with $O(^1D)$, leading to a global lifetime currently estimated at $\sim$ 122–131 years (Volk et al., 1997; Prather et al., 2012). Atmospheric N_2O is currently increasing at $\sim 0.8\,\mathrm{ppb\,year^{-1}}$ (http://ds.data.jma.go.jp/gmd/wdcgg/pub/global/globalmean.html), driven by accelerating human perturbation of the nitrogen cycle: in particular, rising application of nitrogen fertilizers (Galloway et al., 2008; Davidson, 2009; Park et al., 2012) and the nonlinear response of soil N_2O emissions to N inputs in excess of crop demands (Shcherbak et al., 2014).

Rates of microbial nitrification and denitrification in soils depend strongly on environmental characteristics such as temperature (Potter et al., 1996), moisture (Bouwman, 1998; Bouwman et al., 2013), availability of reactive nitrogen substrate, and the make-up of the soil microbial community (Butterbach-Bahl et al., 2013), and as a result large uncertainties exist in the spatial and temporal distribution of global N_2O emissions. Long-term flask-based and in situ observations of atmospheric N_2O are available from a number of monitoring networks around the world, along with routine and intensive aircraft observations, and there have been several recent studies employing these data to generate top–down estimates of global N_2O emissions. Huang et al. (2008) derived a global N_2O flux of 14.1–17.1 $\mathrm{Tg\,N\,year^{-1}}$ for 2002–2005 using surface observations from four different surface monitoring networks. Based on aircraft observations from the first two HIAPER Pole-to-Pole Observations (HIPPO) campaigns, Kort et al. (2011) found evidence for large and episodic tropical fluxes. Saikawa et al. (2014) combined surface observations with aircraft- and ship-based measurements to derive regional N_2O emission estimates for five source sectors, and inferred a global flux of $18.1 \pm 0.6\,\mathrm{Tg\,N\,year^{-1}}$ for 2002–2005. Thompson et al. (2014a) used ground- and ship-based observations to estimate regional N_2O emissions and their interannual variability. Their study yielded global fluxes for 1999–2009 that ranged from 17.5 to 20.1 $\mathrm{Tg\,N\,year^{-1}}$, with interannual variability driven largely by fluctuations in tropical and subtropical soil fluxes. A recent intercomparison of top–down inversion results using different transport models gave a comparable range of global fluxes: 16.1–18.7 $\mathrm{Tg\,N\,year^{-1}}$ for 2006–2009 (Thompson et al., 2014c).

Some previous work has found that uncertainties in stratosphere–troposphere exchange (STE) and the associated influx of N_2O-depleted air can give rise to significant uncertainties in N_2O source inversions, depending on the time range and scale over which the emissions are optimized (Nevison et al., 2005; Hirsch et al., 2006; Huang et al., 2008). On the other hand, Thompson et al. (2011) found their a posteriori surface fluxes to be quite insensitive to biases in the N_2O stratospheric loss rate during the first year of a multiyear simulation. They also found that combining surface and aircraft observations could provide some constraint on the magnitude of the stratospheric N_2O sink in a simultaneous source–sink inversion, without increasing errors in the a posteriori N_2O emissions. However, biases in the model STE itself did give rise to regional uncertainties of up to 25 % in the optimized source.

The global observing network for atmospheric N_2O includes flask-based measurements and quasi-continuous in situ instruments, as well as both surface- and airborne sampling platforms. However, a full quantification of the relative utility of these different data sets has not yet been performed. Such information is needed in order to determine (i) the degree to which current observations can be used to constrain N_2O emissions and stratospheric loss, and the comparative value of different observing strategies for doing so; (ii) the spatial and temporal resolution at which N_2O sources and sinks can be constrained by these different data sets; and

(iii) where additional measurements are most needed to advance present understanding of the atmospheric N_2O budget.

In this paper, we introduce a new simulation and inversion framework for atmospheric N_2O using the GEOS-Chem chemical transport model (CTM) and its adjoint. The adjoint-based variational method is advantageous as it allows us to solve for N_2O fluxes at the spatial resolution of the CTM and at any desired time step, thus minimizing any impact from aggregation errors. Here, we apply the model in a simulation environment (i.e., in observing system simulation experiments, or OSSEs) to quantify the N_2O source and sink constraints provided by (i) flask and quasi-continuous surface observations from a number of long-term monitoring networks; (ii) routine flask observations from an instrument platform deployed onboard a commercial aircraft (CARIBIC); and (iii) in situ airborne observations made during a series of intensive pole-to-pole field campaigns (HIPPO). This is the first study to quantify the individual constraints provided by these different observation ensembles. We determine the potential for model errors in the stratospheric loss rate of N_2O to bias the inferred emission estimates, and assess how well N_2O emissions and stratospheric loss can be simultaneously constrained by the above observations. We evaluate the temporal and spatial resolution of emission constraints afforded by the different N_2O observations, and explore the impact of uncertainties in the a priori error estimates on the inferred fluxes. Finally, we apply the above information to identify regions that are under-constrained by the current N_2O observing network, and the downwind locations where new measurements would be most valuable for reducing current uncertainty in the N_2O budget.

2 N_2O simulation in the GEOS-Chem CTM

In this work we implement an N_2O simulation in the GEOS-Chem (http://www.geos-chem.org) global 3-D model of atmospheric chemistry. Analyses presented here use assimilated meteorological data from the NASA Goddard Earth Observing System (GEOS-5), degraded to a horizontal resolution of 4° latitude × 5° longitude and to a vertical grid containing 47 levels from the surface to 0.01 hPa. Transport is calculated on a 30 min time step; a 60 min time step is used for emissions and chemistry. Our simulation period runs from April 2010 to April 2012.

A priori N_2O emissions are grouped into four categories: anthropogenic (including industrial processes, transportation, residential/waste management, and agricultural activities), natural soil fluxes, biomass burning, and oceanic exchange. Annual emissions for anthropogenic activities are obtained from the Emission Database for Global Atmospheric Research (EDGARv4.2; http://edgar.jrc.ec.europa.eu). Within this database there are 12 emission sectors as defined by the IPCC (IPCC, 2006). These sectors are listed

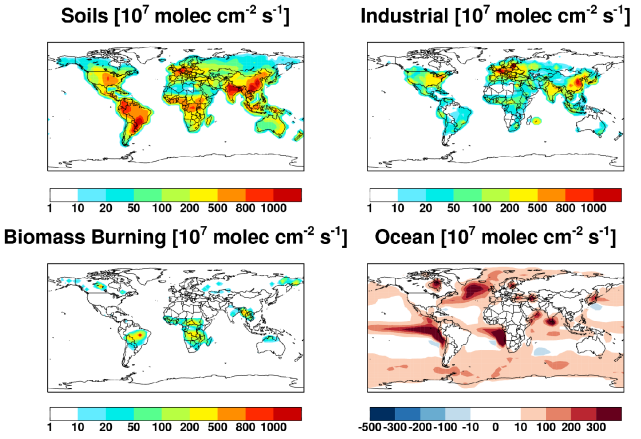

Figure 1. Mean annual N_2O fluxes from soils, industrial activities, biomass burning, and ocean exchange in the GEOS-Chem a priori simulation.

in Table 1, along with the corresponding total emissions for 2008. The overall anthropogenic N_2O flux from EDGARv4.2 is 6.9 Tg N year^{-1}, with 2.4 Tg N year^{-1} from industrial and residential sources and 4.5 Tg N year^{-1} from direct and indirect agricultural emissions. Natural soil emissions of N_2O are computed based on the EDGARv2 database, which provides an annual flux at 1° × 1° resolution for the year 1990 totaling 3.2 Tg N year^{-1}. Biomass burning emissions of N_2O are prescribed monthly based on the Global Fire Emissions Database version 3 (GFEDv3; van der Werf et al., 2010) and total 0.6 Tg N year^{-1} for 2010–2011. Thermal and biogeochemical oceanic fluxes of N_2O are calculated monthly at 4.5° × 3.75° following Jin and Gruber (2003), leading to a net annual global source of 3.5 Tg N year^{-1}. Figure 1 maps the resulting annual flux from soils, industrial activities, biomass burning, and air–sea exchange, with a cumulative annual global source of 14.2 Tg N year^{-1}. We note that this is below the range of current top–down flux estimates (∼ 16 to 20 Tg N year^{-1}) discussed previously.

Stratospheric destruction of N_2O by photolysis and reaction with $O(^1D)$ is calculated using archived monthly 3-D loss frequencies from Global Modeling Initiative (GMI) simulations driven by Modern-Era Retrospective Analysis for Research and Applications (MERRA) meteorological fields (MERRA is also based on GEOS-5). The resulting stratospheric loss gives rise to a 127.5 year lifetime, which is in the range of current estimates (122–131 years, Volk et al., 1997; Prather et al., 2012). This lifetime depends upon the initial mass distribution assumed for N_2O, which we describe below.

Because of the long atmospheric lifetime of N_2O, generating realistic initial conditions is of critical importance for top–down analyses of its sources and sinks. Some previous studies have included initial conditions as part of the state vector for optimization, or prescribed N_2O mass fields from

Table 1. N_2O emissions in the a priori database and their global annual totals.

Sector	IPCC code	Global annual source (Tg N year^{-1})
Agricultural soil[a]	4C + 4D	3.97
Indirect emissions from agriculture[a]	4D3	0.57
Energy manufacturing transformation[a]	1A1 + 1A2 + 1B1b	0.21
Non-road transportation[a]	1A3a + c + d + e	5.0×10^{-2}
Road transportation[a]	1A3b	0.14
Oil production and refineries[a]	1B2a	4.2×10^{-3}
Industrial process and product use[a]	2	0.85
Fossil fuel fires[a]	7A	4.8×10^{-4}
Manure management[a]	4B	0.21
Residential[a]	1A4	0.18
Waste solid and waste water[a]	6	0.24
Indirect N_2O from NO_x and NH_3[a]	7B + 7C	0.45
Total anthropogenic[a]		6.9
Total natural soil[b]		3.2
Total biomass burning[c]		0.6
Total net ocean[d]		3.5

[a] From EDGARv4.2 for 2008. [b] From EDGARv2 for 1990. [c] From GFEDv3 (van der Werf et al., 2010).
[d] From Jin and Gruber (2003).

simulations that have reached a pseudo steady state. We instead construct an initial 3-D N_2O field using global observations for March 2010 (Fig. 2), 1 month prior to the start of our optimization window. This timing is chosen to accommodate a brief model spin-up that smooths any artificial horizontal gradients prescribed in the initial conditions. Initial tropospheric concentrations are computed from NOAA Carbon Cycle and Greenhouse Gases (CCGG) flask observations (described below) averaged monthly and zonally at 4° resolution. These mixing ratios are then assumed uniform from the surface to the tropopause. Above 100 hPa, our initial conditions are based on monthly mean (March 2010) N_2O profiles measured by the Microwave Limb Sounder (MLS) onboard the EOS Aura satellite (Lambert et al., 2007) interpolated onto the GEOS-Chem horizontal and vertical grid. Where needed, we then perform a linear interpolation between the tropopause and 100 hPa.

3 Inversion setup and verification

We use a 4D-Var inversion framework to solve for spatially resolved, monthly N_2O fluxes based on the atmospheric measurements described next (Sect. 4). Optimal fluxes are derived by minimizing the cost function, $J(\boldsymbol{p})$, which contains contributions from the error-weighted model–measurement differences and a penalty term:

$$J(\boldsymbol{p}) = \frac{1}{2}\sum_{c\in\Omega}(\boldsymbol{c}-\boldsymbol{y})^T\mathbf{S}_y^{-1}(\boldsymbol{c}-\boldsymbol{y}) + \frac{1}{2}\gamma\left(\boldsymbol{p}-\boldsymbol{p}_\mathrm{a}\right)^T\mathbf{S}_\mathrm{a}^{-1}(\boldsymbol{p}-\boldsymbol{p}_\mathrm{a}). \quad (1)$$

Here, $\boldsymbol{p}$ is the vector of parameters to be optimized, $\boldsymbol{p}_\mathrm{a}$ is the initial (a priori) value of those parameters, $\boldsymbol{y}$ is a set of observations, $\boldsymbol{c}$ is a vector containing the model-simulated concentrations, $\mathbf{S}_y$ and $\mathbf{S}_\mathrm{a}$ are the observational and a priori error covariance matrices, respectively, Ω is the time and space domain of the observations, and γ is a regularization parameter (set here to 1.0).

In this study, $\boldsymbol{p}$ contains monthly scaling factors for the terrestrial and oceanic emissions of N_2O and for stratospheric loss frequencies. The adjoint model calculates the gradient of the cost function with respect to this state vector, $\nabla_p J(\boldsymbol{p})$, and employs a quasi-Newton minimization routine to iteratively minimize $J(\boldsymbol{p})$ (Zhu et al., 1994; Byrd et al., 1995). Scale factors for emissions are optimized on the $4° \times 5°$ GEOS-Chem grid, while those for the stratospheric loss frequencies are aggregated over the vertical extent of the stratosphere and into eight latitude bands of 22.5°. For the 2-year inversion, this results in a state vector with 79 488 elements for emissions and 192 elements for stratospheric loss. We use a lower bound of zero in the optimization routine to avoid a solution containing negative scaling factors and an upper bound of 10 that was found to improve optimization performance. Use of the lower bound corresponds to an implicit assumption that the sign of the a priori N_2O flux in each location is correct, while the upper bound assumes that the a priori emissions are not biased low by more than a factor of

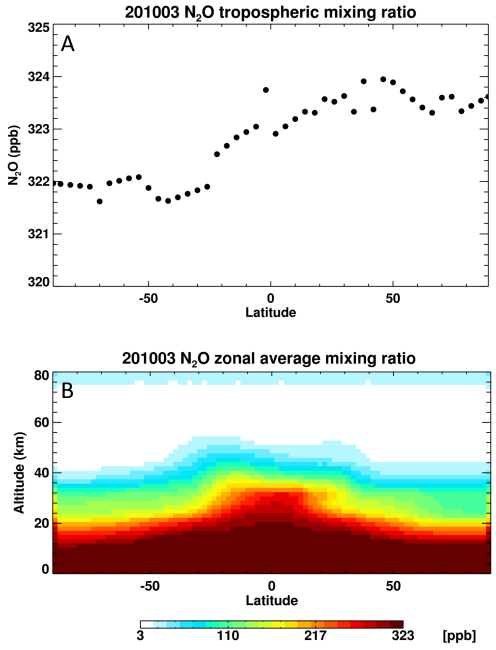

Figure 2. Initial model N_2O field for March 2010. Shown are the **(a)** tropospheric N_2O mixing ratios, and **(b)** zonal mixing ratio cross section.

10. Such bounds are not problematic for the synthetic experiments presented here, but would affect real inversions if those assumptions were violated.

We assume 100 % uncertainty in the a priori emissions (for any given grid square and month) and in the stratospheric loss frequencies, and impose horizontal correlation length scales for emissions of 500 km over land and 1000 km over ocean, following Thompson et al. (2011, 2014a). The observational error covariance matrix contains contributions from the measurement uncertainty (typically 0.4 ppb; see next section for details) and from model transport errors. We estimate the latter from the variance in modeled N_2O mixing ratios across all grid boxes adjacent to that containing a given observation. This results in mean errors of 0.2 ppb at the surface and 2–8 ppb at aircraft cruising altitudes.

The adjoint modules for optimizing N_2O emissions and stratospheric loss were verified by comparing adjoint and finite difference sensitivities calculated for each atmospheric column with no horizontal transport. We find good agreement between adjoint and finite difference sensitivities for both emissions and stratospheric loss scaling factors (Fig. S1 in the Supplement), demonstrating the accuracy of the N_2O adjoint code. Propagation of adjoint sensitivities through horizontal transport in the GEOS-Chem adjoint has been verified previously (Henze et al., 2007). The GEOS-Chem adjoint has been used for a wide range of research applications, such as constraining sources of aerosols (Henze et al., 2007, 2009; Kopacz et al., 2011; Wang et al., 2012; Xu et al., 2013), CO (Kopacz et al., 2009, 2010), NH_3 (Zhu et al., 2013), O_3 (Zhang et al., 2009; Parrington et al., 2012), and methanol (Wells et al., 2014), and to assess the impact of different types of observations on CO source inversions (Jiang et al., 2011, 2013).

4 Global observations of atmospheric N_2O

Below, we apply GEOS-Chem and its adjoint to assess the N_2O source and sink constraints provided by the current suite of global observations. We include in this assessment several long-term surface monitoring networks and two aircraft platforms. A full list of the surface observation sites can be found in Table 2, and their locations are mapped in Fig. 3. The majority of the surface observations are from discrete air samples collected approximately weekly in flasks at 77 sites in the NOAA CCGG program (Dlugokencky et al., 1994), which are analyzed using a gas chromatograph with an electron capture detector and reported on the NOAA 2006A calibration scale. We also use flask measurements from six sites in the Commonwealth Scientific and Industrial Research Organisation (CSIRO) network (also on the NOAA 2006A scale; Francey et al., 1996; Cooper et al., 1999), five sites in the Environment Canada (EC) network (NOAA 2006 scale), and one National Institute of Water and Atmospheric research (NIWA) site (NOAA 2006A scale). We assume a measurement uncertainty of 0.4 ppb for all of the above flask measurements, based on recommendations from the data providers. Hourly averages of quasi-continuous measurements are employed from six sites in the NOAA Chromatograph for Atmospheric Trace Species (CATS) network, six sites in the Advanced Global Atmospheric Gases Experiment (AGAGE) network (Prinn et al., 2000), and the University of Minnesota tall tower Trace Gas Observatory (KCMP tall tower, MB, USA; 44.68° N, 93.07° W) site (Griffis et al., 2013). Measurements from the AGAGE network are reported on the SIO-98 scale, and have a reported uncertainty of 0.2 % (0.6 ppb). Measurements at the KCMP tall tower and those in the CATS network (both on the NOAA 2006A scale) have uncertainties of about 1.0 and 0.3 ppb, respectively.

Extensive airborne measurements of N_2O are available from the CARIBIC observatory (Brenninkmeijer et al., 2007). CARIBIC provides flask measurements from a commercial Lufthansa aircraft, with data available for 79 flights between Frankfurt, Germany, and a number of other cities around the world (Fig. 3) during the time period of our optimization. These observations have an uncertainty of about 0.35 ppb and are reported on the NOAA 2006 scale (Schuck et al., 2009). Since the CARIBIC observatory is operated on a passenger aircraft, the majority of measurements are taken at a cruising altitude of 9–12 km: about 50 % are in the lowermost stratosphere (in general those at higher latitudes, depending on synoptic conditions), with the remainder sampling the upper troposphere (Assonov et al., 2013; Umezawa et al., 2014).

Table 2. Sites of surface flask and in situ N_2O observations used in this study.

Location	Latitude	Longitude	Network*	Measurement type	Measurement scale
Arrival Heights, Antarctica	−77.80	166.67	NIWA	Flask	NOAA 2006A
Alert, Nunavut, Canada	82.45	−62.51	CCGG	Flask	NOAA 2006A
Argyle, Maine, USA	45.04	−68.68	CCGG	Flask	NOAA 2006A
Ascension Island	−7.97	−14.40	CCGG	Flask	NOAA 2006A
Assekrem, Algeria	23.26	5.63	CCGG	Flask	NOAA 2006A
Terceira Island, Azores	38.77	−27.38	CCGG	Flask	NOAA 2006A
Baltic Sea, Poland	55.35	17.22	CCGG	Flask	NOAA 2006A
Boulder Atmospheric Observatory, Colorado, USA	40.05	−105.00	CCGG	Flask	NOAA 2006A
Baring Head, New Zealand	−41.41	174.87	CCGG	Flask	NOAA 2006A
Bukit Kototabang, Indonesia	−0.20	100.32	CCGG	Flask	NOAA 2006A
St. David's Head, Bermuda	32.37	−64.65	CCGG	Flask	NOAA 2006A
Tudor Hill, Bermuda	32.27	−64.88	CCGG	Flask	NOAA 2006A
Barrow, Alaska, USA	71.32	−156.61	CCGG, CATS	Flask, in situ	NOAA 2006A
Black Sea, Constanţa, Romania	44.18	28.67	CCGG	Flask	NOAA 2006A
Cold Bay, Alaska, USA	55.21	−162.72	CCGG	Flask	NOAA 2006A
Cape Ferguson, Australia	−19.28	147.05	CSIRO	Flask	NOAA 2006A
Cape Grim, Tasmania, Australia	−40.68	144.69	CCGG, AGAGE	Flask, in situ	NOAA 2006A, SIO-98
Churchill, Manitoba, Canada	58.75	−94.07	EC	Flask	NOAA 2006
Christmas Island	1.70	−157.15	CCGG	Flask	NOAA 2006A
Cape Rama, India	15.08	73.83	CSIRO	Flask	NOAA 2006A
Crozet Island	−46.43	51.85	CCGG	Flask	NOAA 2006A
Casey Station, Antarctica	−66.28	110.53	CSIRO	Flask	NOAA 2006A
Drake Passage	−59.00	−64.69	CCGG	Flask	NOAA 2006A
Easter Island	−27.16	−109.43	CCGG	Flask	NOAA 2006A
Estevan Point, British Columbia, Canada	49.38	−126.55	EC	Flask	NOAA 2006
East Trout Lake, Saskatchewan, Canada	54.33	−104.98	EC	Flask	NOAA 2006
Fraserdale, Ontario, Canada	49.88	−81.57	EC	Flask	NOAA 2006
Mariana Islands, Guam	13.39	144.66	CCGG	Flask	NOAA 2006A
Gunn Point, Australia	−12.25	131.05	CSIRO	Flask	NOAA 2006A
Halley Station, Antarctica	−75.61	−26.21	CCGG	Flask	NOAA 2006A
Hohenpeissenberg, Germany	47.80	11.02	CCGG	Flask	NOAA 2006A
Hegyhátsál, Hungary	46.95	16.65	CCGG	Flask	NOAA 2006A
Stórhofdi, Vestmannaeyjar, Iceland	63.40	−20.29	CCGG	Flask	NOAA 2006A
Izaña, Tenerife, Canary Islands	28.31	−16.50	CCGG	Flask	NOAA 2006A
Jungfraujoch, Switzerland	46.55	7.99	AGAGE	In situ	SIO-98
Key Biscayne, Florida, USA	25.67	−80.16	CCGG	Flask	NOAA 2006A
Cape Kumukahi, Hawaii, USA	19.52	−154.82	CCGG	Flask	NOAA 2006A
Park Falls, Wisconsin, USA	45.95	−90.27	CCGG	Flask	NOAA 2006A
Lac La Biche, Alberta, Canada	54.95	−112.45	CCGG	Flask	NOAA 2006A
Lulin, Taiwan	23.47	120.87	CCGG	Flask	NOAA 2006A
Lampedusa, Italy	35.52	12.62	CCGG	Flask	NOAA 2006A
Mawson Station, Antarctica	−67.62	62.87	CSIRO	Flask	NOAA 2006A
Mace Head, Ireland	53.33	−9.90	CCGG, AGAGE	Flask, in situ	NOAA 2006A, SIO-98
Sand Island, Midway Islands	28.21	−177.38	CCGG	Flask	NOAA 2006A
Mt. Kenya, Kenya	−0.06	37.30	CCGG	Flask	NOAA 2006A
Mauna Loa, Hawaii, USA	19.54	−155.58	CCGG, CATS	Flask, in situ	NOAA 2006A, NOAA 2006A
Macquarie Island, Australia	−54.48	158.97	CSIRO	Flask	NOAA 2006A
Gobabeb, Namibia	−23.58	15.03	CCGG	Flask	NOAA 2006A
Niwot Ridge, Colorado, USA	40.05	−105.55	CCGG, CATS	Flask, in situ	NOAA 2006A, NOAA 2006A
Ochsenkopf, Germany	50.03	11.81	CCGG	Flask	NOAA 2006A
Pallas–Sammaltunturi, Finland	67.97	24.12	CCGG	Flask	NOAA 2006A
Pacific Ocean, Equator	0.00	−155.00	CCGG	Flask	NOAA 2006A
Pacific Ocean, 5° N	5.00	−151.00	CCGG	Flask	NOAA 2006A
Pacific Ocean, 10° N	10.00	−149.00	CCGG	Flask	NOAA 2006A
Pacific Ocean, 15° N	15.00	−145.00	CCGG	Flask	NOAA 2006A
Pacific Ocean, 20° N	20.00	−141.00	CCGG	Flask	NOAA 2006A
Pacific Ocean, 25° N	25.00	−139.00	CCGG	Flask	NOAA 2006A
Pacific Ocean, 30° N	30.00	−135.00	CCGG	Flask	NOAA 2006A
Pacific Ocean, 5° S	−5.00	−159.00	CCGG	Flask	NOAA 2006A
Pacific Ocean, 10° S	−10.00	−161.00	CCGG	Flask	NOAA 2006A
Pacific Ocean, 15° S	−15.00	−171.00	CCGG	Flask	NOAA 2006A
Pacific Ocean, 20° S	−20.00	−174.00	CCGG	Flask	NOAA 2006A
Pacific Ocean, 25° S	−25.00	−171.00	CCGG	Flask	NOAA 2006A
Pacific Ocean, 30° S	−30.00	−176.00	CCGG	Flask	NOAA 2006A
Pacific Ocean, 35° S	−35.00	180.00	CCGG	Flask	NOAA 2006A

Table 2. Continued.

Location	Latitude	Longitude	Network*	Measurement type	Measurement scale
Palmer Station, Antarctica	−64.92	−64.00	CCGG	Flask	NOAA 2006A
Point Arena, California, USA	38.96	−123.74	CCGG	Flask	NOAA 2006A
Ragged Point, Barbados	13.17	−59.43	CCGG, AGAGE	Flask, in situ	NOAA 2006A, SIO-98
Beech Island, South Carolina, USA	33.41	−81.83	CCGG	Flask	NOAA 2006A
Mahe Island, Seychelles	−4.68	55.53	CCGG	Flask	NOAA 2006A
Sable Island, Nova Scotia, Canada	43.93	−60.02	EC	Flask	NOAA 2006
Southern Great Plains, Oklahoma, USA	36.61	−97.49	CCGG	Flask	NOAA 2006A
Shemya Island, Alaska, USA	52.71	174.13	CCGG	Flask	NOAA 2006A
Tutuila, American Samoa	−14.25	−170.56	CCGG, CATS	Flask, in situ	NOAA 2006A, NOAA 2006A
South Pole, Antarctica	−89.98	−24.80	CCGG, CATS	Flask, in situ	NOAA 2006A, NOAA 2006A
Schauinsland, Germany	47.92	7.92	AGAGE	In situ	SIO-98
Sutro Tower, California, USA	37.76	−122.45	CCGG	Flask	NOAA 2006A
Summit, Greenland	72.60	−38.42	CCGG, CATS	Flask, in situ	NOAA 2006A, NOAA 2006A
Syowa Station, Antarctica	−69.01	39.59	CCGG	Flask	NOAA 2006A
Tae-ahn Peninsula, Korea	36.74	126.13	CCGG	Flask	NOAA 2006A
Tierra Del Fuego, Argentina	−54.85	−68.31	CCGG	Flask	NOAA 2006A
KCMP tall tower, Minnesota, USA	44.68	−93.07		In situ	NOAA 2006A
Trinidad Head, California, USA	41.05	−124.15	CCGG, AGAGE	Flask, in situ	NOAA 2006A, SIO-98
Wendover, Utah, USA	39.90	−113.72	CCGG	Flask	NOAA 2006A
Ulaan-Uul, Mongolia	44.45	111.10	CCGG	Flask	NOAA 2006A
West Branch, Iowa, USA	41.73	−91.35	CCGG	Flask	NOAA 2006A
Walnut Grove, California, USA	38.27	−121.49	CCGG	Flask	NOAA 2006A
WIS Station, Negev Desert, Israel	30.86	34.78	CCGG	Flask	NOAA 2006A
Moody, Texas, USA	31.32	−97.33	CCGG	Flask	NOAA 2006A
Mt. Waliguan, China	36.29	100.90	CCGG	Flask	NOAA 2006A
Western Pacific Cruise	−30.00 to 30.00	136.80 to 168.00	CCGG	Flask	NOAA 2006A
Ny-Ålesund, Svalbard, Norway	78.91	11.89	CCGG	Flask	NOAA 2006A

* CCGG: NOAA Carbon Cycle and Greenhouse Gases program; EC: Environment Canada; NIWA: National Institute of Water and Atmospheric research; CATS: NOAA Chromatograph for Atmospheric Trace Species; AGAGE: Advanced Global Atmospheric Gases Experiment.

High-frequency airborne N_2O measurements were made by quantum cascade laser spectroscopy (QCLS) during the HIPPO campaigns (Wofsy, 2011; flight tracks mapped in Fig. 3). Three of the five HIPPO deployments took place during our optimization window: HIPPO III (24 March–16 April 2010), HIPPO IV (14 June–11 July 2011), and HIPPO V (9 August–9 September 2011), totaling 33 flights over the April 2010–April 2012 time frame. Measurements are reported on the NOAA 2006 scale (Kort et al., 2011). The HIPPO flights range from pole-to-pole while profiling the atmosphere from the surface to the tropopause at regular intervals. Unlike the other available data sets, which provide recurrent measurements at discrete locations or along specific flight paths, the HIPPO data sets provide $\sim$ 1-month global cross sections of atmospheric concentration.

The use of different calibration scales results in offsets between different networks measuring N_2O, which may also vary with time. Because variability in atmospheric N_2O is low, these offsets can have a significant impact on the a posteriori solution. As the results presented here involve synthetic observations at the time and location of the real observations, we do not consider the impact of these offsets on inferred N_2O emissions and stratospheric loss. However, for inversions employing real N_2O measurements, we calculate offsets at collocated sites to adjust those measurements that are not reported on the NOAA 2006A scale.

5 Evaluating constraints on N_2O emissions and stratospheric loss using pseudo observations

In this section we perform a range of pseudo observation tests to determine how well N_2O sources (and sinks) can be quantified, and at what space–time resolution, based on the observing network described above. In these tests, we sample the model at the time and location of each observation to generate pseudo observations. A subset of tests were carried out with observational (measurement + transport) noise added to the synthetic observations, and these yielded the same results as the tests with no noise. We then perform a 2-year inversion in which we assimilate pseudo observations generated for the surface network, CARIBIC flights, or HIPPO flights. Our state vector contains monthly scaling factors for emissions, stratospheric loss frequencies, or both. We start with a spatially uniform incorrect a priori value for these scaling factors; this bias is temporally uniform in most tests, though later we also test the impact of a seasonally varying emission bias. The degree to which the optimization converges to the true value of 1.0 for each grid cell and month gives a measure of the ability of the observations to correct for model biases in these processes. Section 5.1 presents tests in which we optimize emissions using the three observational data sets, Sect. 5.2 contains tests in which we optimize stratospheric loss frequencies alone or jointly with emissions, and Sect. 5.3 describes tests in which we optimize emissions with

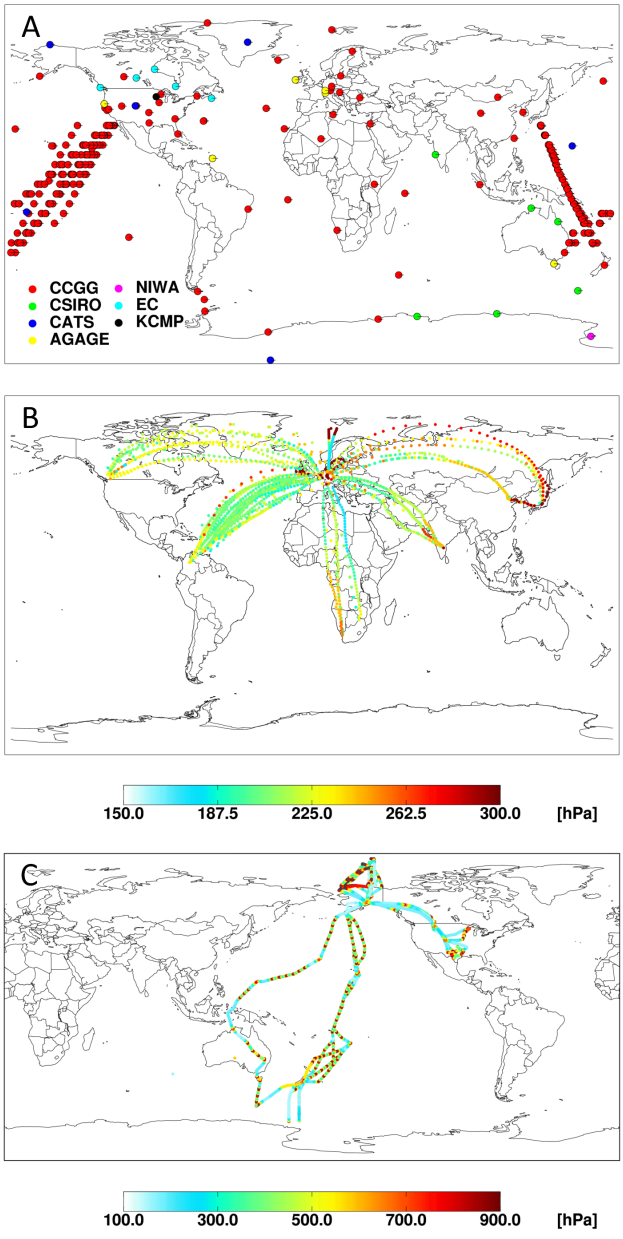

Figure 3. Global observing network for atmospheric N_2O. Shown are the locations of **(a)** surface observations, **(b)** CARIBIC aircraft observations, and **(c)** HIPPO aircraft observations. The CARIBIC and HIPPO flights are shaded by the pressure at which the observations were made. Color scales differ between **(b)** and **(c)** to show the range of vertical sampling in each case.

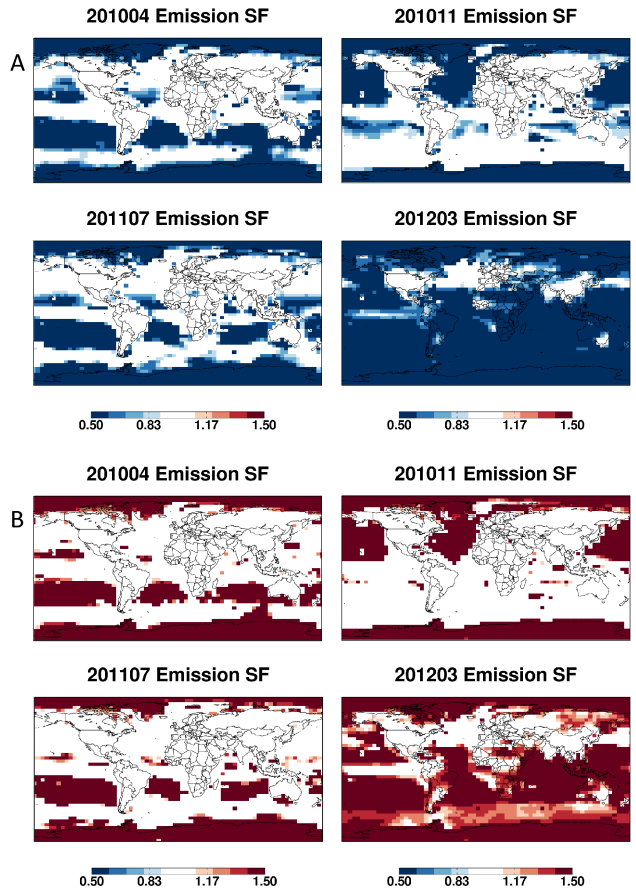

Figure 4. Pseudo observation tests optimizing N_2O emissions on the basis of surface observations. Shown are a posteriori emission scaling factors using an a priori guess of either **(a)** 0.5 or **(b)** 1.5, where the true value is 1.0. Results are shown for April 2010 (month 1 of the inversion window), November 2010 (month 8), July 2011 (month 16), and March 2012 (month 24).

a seasonal a priori bias imposed. A full list of all pseudo observation tests performed is given in Table 3.

5.1 Constraints on N_2O emissions

Figure 4 shows the results of synthetic inversions in which we optimize emissions using surface-based pseudo observations as described above. Here we impose a time invariant a priori emission bias of $\pm 50\,\%$ across all land and ocean grid cells, while keeping the stratospheric loss rates fixed at their true model values. We see that for the first ~ 20 months of the optimization window, the surface-based inversion is able to correct the imposed bias over most land and ocean regions that have a significant flux. However, we will show later that this does not mean current observations can fully constrain the spatial distribution of N_2O emissions at the $4° \times 5°$ resolution shown in Fig. 4.

Overall, the solution is of comparable quality whether we start with a high or low a priori bias, with some minor distinctions: the test with the positive initial bias performs slightly better over oceans and in later months of the simulation, and also converges more quickly (5 iterations versus 10 for the test with a low initial bias). However, the situation is very different when no upper bound is imposed on the solution. In this case, when given a low initial bias the optimization tends to overshoot the truth in high-flux regions while under-

Table 3. Global annual N_2O a posteriori source for all pseudo observation tests.

Observations	State vector	Initial bias	A posteriori flux ($Tg\,N\,year^{-1}$)[a]	A posteriori sink ($Tg\,N\,year^{-1}$)[b]
Surface	Emissions	0.5, 1.5	14.16, 14.25	–
CARIBIC	Emissions	0.5, 1.5	13.82, 14.72	–
HIPPO	Emissions	0.5, 1.5	14.12, 14.27	–
Surface	Emissions + strat. loss frequencies	0.5, 1.5	14.04, 14.84	7.73, 24.91
CARIBIC	Emissions + strat. loss frequencies	0.5, 1.5	13.63, 15.40	6.13, 19.72
HIPPO	Emissions + strat. loss frequencies	0.5, 1.5	14.00, 14.74	7.65, 22.60
Surface	Strat. loss frequencies	0.5, 1.5		12.02, 12.93
CARIBIC	Strat. loss frequencies	0.5, 1.5		10.09, 14.66
HIPPO	Strat. loss frequencies	0.5, 1.5		10.60, 13.99
CARIBIC (no transport error)	Emissions + strat. loss frequencies	0.5	14.16	9.94
HIPPO (no transport error)	Emissions + strat. loss frequencies	0.5	14.14	11.39
CARIBIC (no transport error)	Strat. loss frequencies	0.5		11.57
HIPPO (no transport error)	Strat. loss frequencies	0.5		12.03
Surface	Emissions	Seasonal	13.63	
CARIBIC	Emissions	Seasonal	13.59	
HIPPO	Emissions	Seasonal	13.44	

[a] True model flux is $14.16\,Tg\,N\,year^{-1}$. [b] True model stratospheric sink is $12.1\,Tg\,N\,year^{-1}$.

estimating the truth in low-flux regions. Imposing both lower and upper bounds on the inverse solution (in this case, 0 and 10) is thus important to ensure a consistent solution across high and low initial bias scenarios.

Figure 4 also indicates that during the last several months of the optimization window there is inadequate forcing for the inversion to completely correct for the initial emission biases, particularly over the Southern Hemisphere. This is largely due to the timescale required to transport N_2O between source regions and receptor locations – in the Southern Hemisphere observing stations are sparse and distant from major N_2O sources. As a result, there are relatively few subsequent observations that are influenced by biases imposed towards the end of the optimization window.

Figure 5 shows zonally integrated, annual a posteriori emissions from synthetic inversions using surface, CARIBIC, or HIPPO pseudo observations. In each case the state vector for optimization includes monthly emission scale factors on the model grid (but not stratospheric loss rates), and an initial bias of $\pm 50\,\%$ is applied to emissions in all grid boxes. Results are shown only for the first year of the optimization period since (as shown) the inversion has less ability to retrieve the true emissions in the succeeding months; there are also no HIPPO observations during the last 6 months of the simulation. As discussed, the surface data provide a good correction to the imposed a priori error in N_2O emissions when starting with both high and low initial biases, and can accurately retrieve zonally integrated emissions in the Northern and Southern hemispheres.

We see in Fig. 5 that inversions based on the HIPPO data are also able to capture the zonal distribution of N_2O emissions. For the high-bias test (a priori emissions scaling factor of 1.5), the inversion results are very similar to those obtained using the surface data. For the low-bias test, the a posteriori emissions retain a low bias over the Southern Ocean, and overshoot slightly where emissions peak in both hemispheres. On the other hand, the CARIBIC measurements lead to substantially different a posteriori fluxes between the high- and low-bias tests: the inversion with the high initial bias returns the true zonal distribution of emissions quite well, whereas the test with the low initial bias leads to an overestimate of emissions from 20 to 30° N and an underestimate elsewhere. We find through these tests that each data set can independently resolve the global annual flux to within 5 % of the true value (Table 3).

Based on these experiments, we conclude that relatively sparse observations in the upper troposphere and lowermost stratosphere, such as those from CARIBIC, are sufficient to correct a prior bias in the global annual N_2O emissions, but do not provide as robust a constraint on the zonal distribution of those emissions. The pole-to-pole HIPPO observations, with their extensive vertical profiling from the upper troposphere to the boundary layer, provide a stronger constraint on the zonal distribution of annual emissions despite the fact that they do not cover the full time period of our optimization. This is because the long lifetime of N_2O allows emissions perturbations to impact concentrations far from source regions 2–6 months after the perturbation (Thompson et al., 2014a). Of the three networks examined here (surface, CARIBIC, and HIPPO) in isolation, the regular surface measurements provide the best correction of annual emission biases.

The above OSSEs were performed based on an initial fractional emission bias that is uniform in space and time (i.e., a

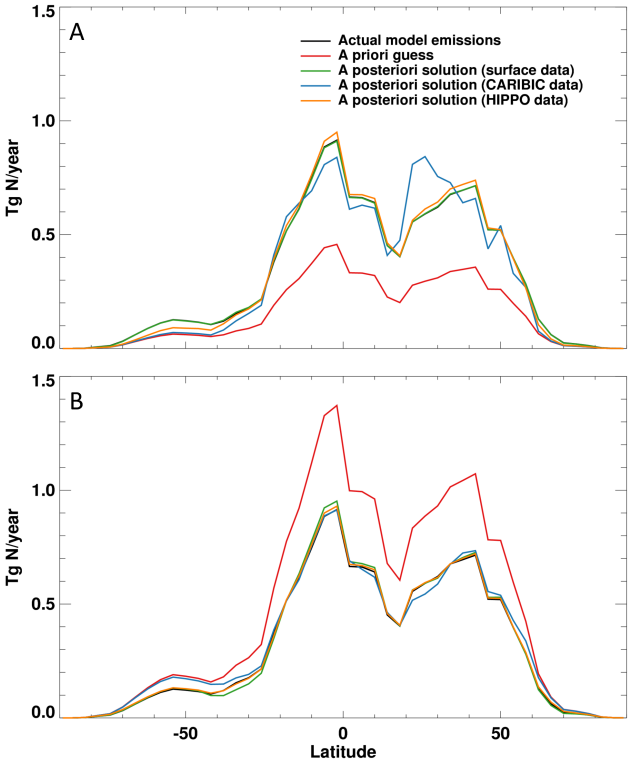

Figure 5. Pseudo observation tests optimizing N_2O emissions. Shown are zonally integrated annual emissions for the first year of the simulation (April 2010–March 2011) starting with an a priori scaling factor of **(a)** 0.5 and **(b)** 1.5, where the true value is 1.0. Actual model emissions are shown in black, model emissions scaled by the a priori guess are shown in red, and a posteriori emissions obtained using surface data, CARIBIC data, and HIPPO data are shown in green, blue, and orange, respectively.

priori emissions set everywhere to $0.5\times$ or $1.5\times$ the true model values). As we will see later, emission biases that vary in space or time are much more difficult to resolve, due to the sparse observing network combined with the long atmospheric lifetime of N_2O.

5.2 Stratospheric loss of N_2O: constraints from the observing network and impact on source inversions

An important finding from previous work is that N_2O emission estimates derived from surface concentration measurements can be biased by model errors in the stratospheric sink of N_2O (Thompson et al., 2011). Here, we explore the potential for the airborne observations provided by CARIBIC and HIPPO, in conjunction with the surface network, to simultaneously constrain N_2O sinks as well as sources. To this end, we perform a series of synthetic inversions with a prior bias imposed on the stratospheric loss frequencies for N_2O (aggregated to eight equal latitude bands), and assess the degree to which we can correct for errors in the N_2O sink (given a fixed N_2O source) or both the source and sink of N_2O (simultaneously). As previously, a priori scaling factors of either 0.5 or 1.5 are applied in each location and month, and we attempt to retrieve the true value of 1.0 in each case.

Figure 6 shows the resulting a posteriori scaling factors for stratospheric loss frequencies when N_2O emissions are held fixed (and equal to their "true" values). We can see that each observational data set provides some information to correct for biases in the loss frequencies in the first year of the simulation. Stratospheric loss of N_2O in the second (i.e. final) year of the inversion does not significantly affect N_2O mixing ratios at the observation locations, as the timescale for mixing from the upper stratosphere (where most of the N_2O loss occurs) to the troposphere is 1–2 years (Salstein, 1995). As a result, the corresponding a posteriori scale factors do not diverge significantly from their a priori values.

For the inversion using surface data, the optimized annual global sink in the first year of the simulation is very close to the true value (Table 3), but the loss frequencies are only adjusted throughout the first year in the tropics. In the extratropics, they adjust primarily during the summer months. The extratropical timing corresponds to the observed seasonal minimum of N_2O at these latitudes (Nevison et al., 2011). At their peaks, retrieved values in the Southern Hemisphere approach the truth, whereas in the Northern Hemisphere they slightly overshoot the true sink. A posteriori values near the poles remain close to the a priori in both hemispheres. Solutions achieved using HIPPO or CARIBIC data are spatially similar to those obtained with the surface observations, although the optimized global sink for both is biased low (by 13–17 %, Table 3) due to weaker forcing (fewer total observations, higher observation uncertainty). Therefore, while all the observations provide some correction of biases in the global stratospheric sink of N_2O given known surface fluxes (with the surface data providing the strongest constraint), they provide limited information on the spatial and temporal distribution of that sink.

Also shown in Fig. 6 are the a posteriori scaling factors for stratospheric loss frequencies of N_2O when both the source and sink are optimized simultaneously, and given an initial 50 % low bias for each. In these tests, the sink does not return to the true value (Table 3); for the inversions using CARIBIC and HIPPO it actually moves slightly in the opposite direction (i.e., further from the truth than the a priori) due to the forcing imposed by the source bias. In other words, the inversion is not able to resolve a bias in N_2O emissions from a bias in the sink. Despite this behavior, the spatial distribution of the derived scaling factors for N_2O emissions (not shown) closely matches that obtained with a fixed ("true") stratospheric sink, and the annual a posteriori emission flux is within 5 % of the truth (Table 3) for all tests except the high-bias test using CARIBIC pseudo data. Therefore, on the 1–2 year timescale of our optimization, and given accurate initial conditions (in our case, based on interpolated measurements), the forcing provided by the surface and aircraft data used here is dominated by N_2O emissions. As a result, a

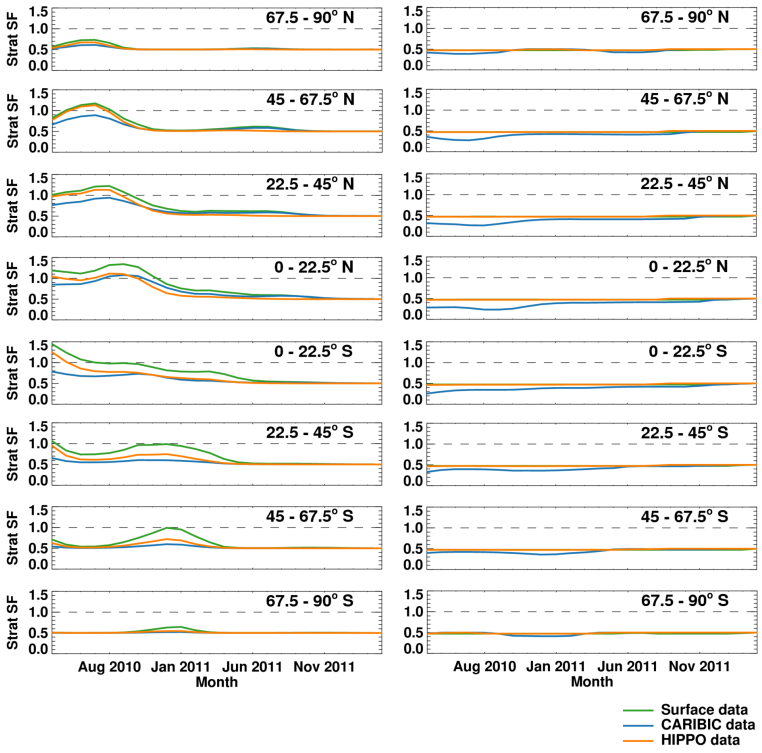

Figure 6. Pseudo observation tests optimizing N_2O stratospheric loss frequencies. Shown are a posteriori scaling factors (SF) for stratospheric loss frequencies in each of eight equal latitude bands for pseudo observation tests in which we optimize solely the stratospheric loss frequencies (left panels) or the emissions and stratospheric loss frequencies jointly (right panels). The latitude range of each band is indicated in the upper right hand corner of each panel. The true model value (1.0) is indicated by the black dashed line; each test started with a priori SF of 0.5 for each latitude band. Results obtained using surface data, CARIBIC data, and HIPPO data are shown in green, blue, and orange, respectively.

model bias of up to 50 % in the stratospheric loss frequencies for N_2O will have a minimal impact on the inferred emissions given the inversion framework employed here.

Thompson et al. (2011) also examined the feasibility of constraining stratospheric loss rates of N_2O using aircraft observations, but assumed zero model transport error in the observational error covariance matrix. We find that proper treatment of this error has a dramatic effect on the ability of the inversion framework to simultaneously retrieve emissions and stratospheric loss rates of N_2O. In the tests above, the model transport error was estimated based on the variance in N_2O mixing ratios in the grid boxes adjacent to an observation; for aircraft observations near the tropopause, this variability can be an order of magnitude larger than it is near the surface. We find that when we omit the model transport error, the inversion is able to reduce an imposed prior bias in both emissions and stratospheric loss simultaneously, even when those biases have opposing effects on the N_2O burden. As observed above, the same is not true when transport error is accounted for. Our ability to quantify both the emissions and chemistry of N_2O based on aircraft data therefore depends critically on the accuracy of vertical transport in the model, and on the associated transport error assigned in the inversion. Tracer measurements and correlations from platforms such as CARIBIC can be useful for evaluating this.

Along with the rate of N_2O destruction in the stratosphere, another factor that can affect N_2O source inversions is model uncertainty in the mass flux of air between the stratosphere and troposphere (e.g., Thompson et al., 2014b). Our model framework, employing assimilated meteorology, is not equipped to include this process directly as part of the state vector for optimization. However, we can explore the relative influence of chemistry versus stratosphere–troposphere mixing on the tropospheric N_2O burden (and hence on N_2O source inversions) with the aid of a simple two-box model representing stratospheric and tropospheric reservoirs of N_2O. Such an analysis does not capture seasonal effects, distinct STE mechanisms operating on different timescales, or spatial gradients within the troposphere and stratosphere, but nonetheless does illustrate some key features of the system.

Figure 7 shows the fractional perturbations to the stratospheric and tropospheric burdens of N_2O in the box model that result from (i) a 20 % increase in the global N_2O emission source (E), (ii) a 20 % decrease in the photochemical loss rate of N_2O (k_{chem}), and (iii) a 20 % decrease in the

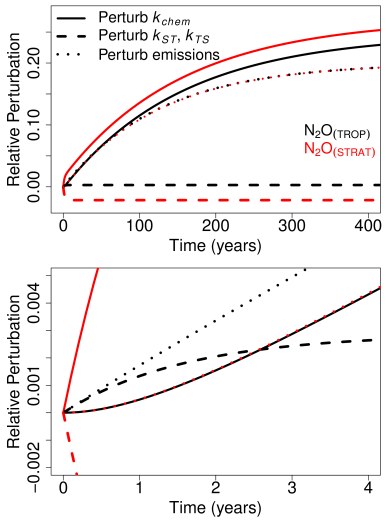

Figure 7. Results from a two-box model illustrating the sensitivity of the tropospheric N_2O burden (and hence source inversions) to the N_2O stratospheric loss rate and to the rate of stratosphere–troposphere exchange. Shown are the relative perturbations to the tropospheric (black lines) and stratospheric (red lines) N_2O burdens resulting from a 20 % change in the N_2O stratospheric loss frequency ("Perturb k_{chem}", solid lines), a 20 % change in the rate of stratosphere–troposphere exchange ("Perturb k_{ST}, k_{TS}", dashed lines), and a 20 % change in emissions ("Perturb emissions", dotted lines). The top panel shows results over a 400-year timescale, while the bottom panel shows the initial 4 years.

stratosphere–troposphere exchange rates (k_{ST} and k_{TS}). For the latter, mass fluxes in both directions are increased proportionately since the (annual, global) k_{ST} / k_{TS} ratio is known from the relative sizes of the troposphere and stratosphere.

The top panel of Fig. 7 shows that on long timescales a perturbation to k_{ST} and k_{TS} has a negligible effect on the tropospheric N_2O burden compared to a perturbation to k_{chem} or E. A given change in k_{chem} or E leads to a similar relative change in the steady-state burden, with an adjustment timescale dictated by the N_2O lifetime ($\sim$ 127 years). In comparison, the effect of a change to k_{TS} and k_{ST} is small in the troposphere. For stratospheric N_2O, the effect of k_{TS} and k_{ST} is somewhat larger and of opposite sign: decreasing k_{TS} and k_{ST} reduces stratospheric N_2O while increasing tropospheric N_2O.

However, on short timescales (as is used for our inversions), the importance of stratosphere–troposphere exchange versus chemistry for tropospheric N_2O is reversed, as the former manifests more quickly. The bottom panel of Fig. 7 indicates that for the first 2 years following a perturbation, the effect of k_{TS} and k_{ST} on the tropospheric N_2O burden is 1.3–29 $\times$ larger (mean: 5.1 $\times$) than the effect of k_{chem}. Over this same time period, Fig. 7 also shows that the effect of a perturbation to k_{TS} and k_{ST} is significant (mean: 0.8 $\times$) relative to a change in E. However, the importance of k_{TS} and k_{ST} versus E will be overstated by the box model as it does not resolve spatial gradients within the troposphere or the location of observations relative to emissions.

Overall, we can see that N_2O source inversions based on the framework employed here will be unaffected by even relatively large model biases in the chemical loss rate of N_2O. The same does not apply to model biases in STE, and these need to be accounted for when evaluating a posteriori source estimates for N_2O (Thompson et al., 2014b) and other long-lived species such as CO_2 (Deng et al., 2015).

5.3 Temporal resolution of N_2O source inversions

The OSSEs in Sect. 5.1 and 5.2 demonstrate that the inversion (and N_2O observing network) has a strong ability to remove model emission biases that are uniform in space and time. However, actual model emission errors are likely to be spatially and temporally dependent. For example, while the a priori natural soil and anthropogenic emissions used here are aseasonal, observations over an agricultural field in Ontario, Canada, indicate that 30–90 % of the annual flux occurs in the non-growing season, mostly as strong pulses driven by soil thawing (Wagner-Riddle et al., 2007). Likewise, analysis of tall tower observations suggest a strong seasonal cycle of soil N_2O emissions associated with the timing of fertilizer application (Miller et al., 2012; Griffis et al., 2013). A key question, therefore, is the following: at what spatial and temporal resolution can global N_2O emissions be quantified based on the current observing network?

To explore the temporal aspect of this question, we performed a test in which we assimilate pseudo observations generated with aseasonal (model truth) emissions, while imposing a simple seasonal bias in the a priori emissions from natural and agricultural soils (50 % higher than model truth from March–August; 50 % lower from September–February). As before, we assimilate surface, CARIBIC, or HIPPO observations, and retrieve monthly scaling factors for terrestrial and oceanic N_2O emissions.

Results of this test indicate that a seasonal, global, emission bias is much more difficult to resolve than is a constant bias based on the current network of surface observations. Zonally integrated emissions (Fig. S2) begin to approach the aseasonal model truth in the Northern Hemisphere during the beginning of the simulation (when the a priori emissions are biased high), but there is almost no correction of the seasonal bias in the latter half of the simulation (when a priori emissions are biased low). Due to the long lifetime of N_2O, any residual high emission bias from the first portion of the simulation leads to positive model–measurement residuals even after the emission bias changes sign. Globally, the result is an annual flux that is biased slightly low ($\sim$ 5 %; Table 3) and with incorrect seasonality.

In areas near measurement sites, however, some seasonal constraints are afforded in the inversion. For example, Fig. 8 shows monthly fluxes at four locations: a site with contin-

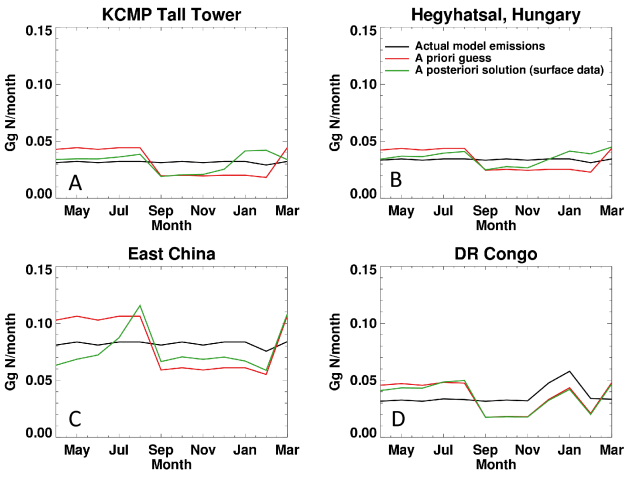

Figure 8. Resolving seasonal emission biases. The panels show the results from an OSSE in which a seasonally dependent a priori emission bias is applied and we test the ability of the inversion to recover the true model fluxes. Results are shown for a site with continuous observations (KCMP tall tower), a site with ∼ weekly flask observations (Hegyhátsál, Hungary), a site with routine flask measurements ∼ 1000 km downwind (East China), and a remote site in the Democratic Republic of Congo (DR Congo). The a priori (red), a posteriori (green), and true model fluxes (black) are plotted for the first year of the simulation (April 2010–March 2011), with the a priori guess for soil emissions biased high in the first half of the inversion period (1.5 ×; March–August) and biased low in the second half (0.5 ×; September–February).

uous observations (KCMP tall tower, MN, USA; 44.68° N, 93.07° W), a site with flask observations (Hegyhátsál, Hungary; 46.95° N, 16.65° E), a location in eastern China that is upwind of surface flask observations (30.0° N, 115° E), and a remote site in the Democratic Republic of Congo (DR Congo; 2.0° N, 30.0° E). At the beginning of the simulation there is a substantial correction of the emission bias at the in situ (KCMP), flask (Hungary), and upwind (East China) sites. During the latter half of the year, when the a priori emissions are biased low, those errors are reduced as a result of the inversion at all three sites, but for the sites with measurements there is a time lag and subsequent overcorrection afterward. There is no significant correction to the biased DR Congo emissions during any point of the year.

Based on the above test, we can conclude that flask and in situ observations provide valuable corrections to seasonal emission biases upwind and in the vicinity of the measurements, though not necessarily on a monthly timescale. However, any seasonal biases arising from errors in model STE may be difficult to separate from such seasonal emission errors. Furthermore, large parts of the world (illustrated by the DR Congo site in Fig. 8) lack any meaningful seasonal constraints on emissions.

5.4 Spatial resolution of N_2O source inversions

The spatial resolution at which current measurements constrain global N_2O emissions in this inversion framework can be inferred from the reduction in emission errors that results from the assimilation. Here, we calculate this relative error reduction from a stochastic estimate of the inverse Hessian of the cost function (Eq. 1). For a reasonably linear model, the inverse Hessian approximates the a posteriori error covariance matrix of the emissions, and can be written

$$(\nabla^2 J(\boldsymbol{x}))^{-1} = (\mathbf{S}_a^{-1} + \mathbf{H}^T \mathbf{S}_y^{-1} \mathbf{H})^{-1} \approx \mathbf{S}_{\text{post}}, \quad (2)$$

where $\mathbf{H}$ is the tangent linear of the forward model, $\mathbf{S}_{\text{post}}$ is the a posteriori error covariance matrix, and $\mathbf{S}_a$ and $\mathbf{S}_y$ are the a priori and observational error covariance matrices, respectively, as in Eq. (1). Following Bousserez et al. (2015), we estimate $\nabla^2 J(\boldsymbol{x})$ using an ensemble (500 members here) of stochastic cost function gradients, each generated by adding Gaussian random noise to the pseudo observations according to the reported uncertainty of each data set. The reduction in $\mathbf{S}_{\text{post}}(i, j)$ relative to $\mathbf{S}_a(i, j)$ for any model grid cell (i, j) then represents the ability of our observing system to remove a random emission error in that location, in the absence of any large-scale source bias.

Figure 9 shows the resulting percent error reduction achieved in each model grid cell using surface, CARIBIC, or HIPPO observations for a given month of our 2-year simulation. Results using surface observations are shown for month 1 (April 2010), but are comparable for all subsequent months. We see appreciable error reduction near sites with continuous observations in North America and Europe, and more modest error reductions in surrounding grid cells, at sites with flask observations, and in the northern Atlantic upwind of Europe. There is little ($< 5\,\%$) error reduction achieved throughout the tropics, Southern Hemisphere, and high latitudes, except near Cape Grim, Australia, where continuous observations are available. The spatial distribution of the error reduction results is similar to the spatial distribution of scaling factor adjustments in a pseudo observation inversion in which a spatially random bias has been applied (not shown).

Figure 9 also shows that the sparse, high altitude CARIBIC observations provide limited information on the spatial distribution of N_2O emissions. Significant error reduction is achieved over western Europe during April 2010, the only month in which measurements were taken in the lower troposphere during special flights dedicated to volcano observation (Rauthe-Schöch et al., 2012). In all other months, measurements occur primarily in the upper troposphere and lower stratosphere and consequently the spatial error reduction is minor (typically $< 1\,\%$).

The spatial information provided by HIPPO observations varies by month according to the flight tracks, and is complementary to that achieved with surface data. For example, during August 2011, we see large error reductions over the cen-

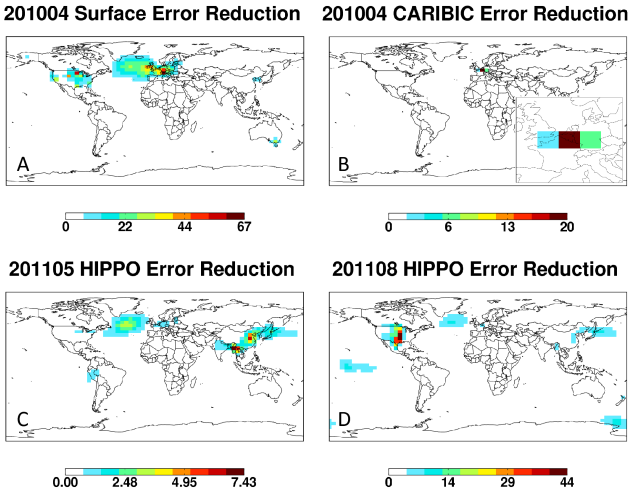

Figure 9. Error reduction (%) in N_2O emissions achievable in selected months using surface **(a)**, CARIBIC **(b)**, and HIPPO **(c** and **d)** measurements. An inset shows regional detail for the CARIBIC results. The relative error reduction is calculated based on a stochastic estimate of the inverse Hessian of the cost function for the inversion, and represents the ability of the observing system to remove a random emission error for each given location in the absence of any large-scale source bias.

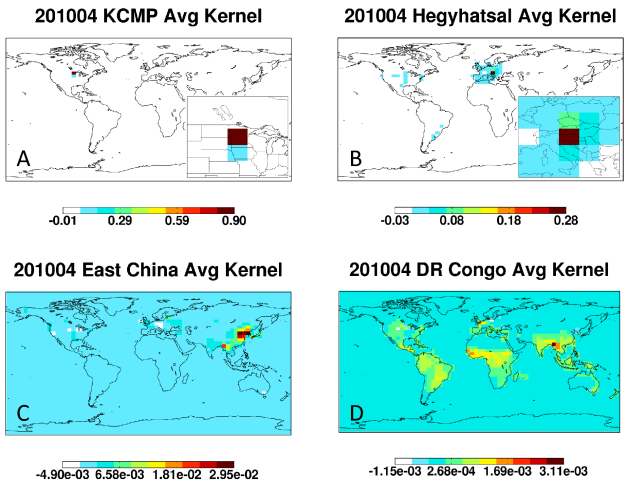

Figure 10. Rows of the averaging kernel for the inversion of N_2O emissions based on surface observations. The results indicate how well emissions in a particular location can be resolved from emissions elsewhere, and are shown for four example sites: **(a)** KCMP tall tower, **(b)** Hegyhátsál, Hungary, **(c)** a grid cell in East China, and **(d)** a grid cell in the Democratic Republic of Congo. Insets show regional detail for the first two sites. KCMP is a site with continuous observations, Hegyhátsál is a site with ∼ weekly flask observations, the East China site is a location with flask observations ∼ 1000 km downwind, and the Congo site is a remote location.

tral USA, as well as some improvement for grid cells in East Asia that are upwind of the HIPPO flight track. Some error reduction is also achieved in these locations for May 2011, despite the fact that no HIPPO flights occurred during this month (the next flights occurred in June). Given the long lifetime of N_2O, measurements in a given month thus provide some location-specific constraints on emissions in prior months. As is the case with the surface observations, however, the HIPPO data provide very little error reduction for emissions throughout the tropics, Southern Hemisphere and high latitudes. While the OSSE tests above showed that our observation and adjoint framework has significant skill in removing uniform model emission biases, we see in Fig. 9 that our current ability to allocate those N_2O emissions spatially around the globe is in fact severely limited relative to the $4° \times 5°$ model resolution used here – and this is true for the airborne as well as the ground-based data sets.

Based on the same stochastic approach used above to calculate the inverse Hessian, we can also calculate the averaging kernel of the inversion. The averaging kernel measures the sensitivity of the inversion to emissions in any given grid square; we can thus use it to determine how well emissions in a given location can be independently resolved from emissions elsewhere. If emissions in one location are completely resolved from those in other grid boxes, the averaging kernel value will be 1.0 in that location and 0 everywhere else. Here, we calculate the averaging kernel rows (based on the surface observations only) for a selected group of locations in key emission regions that vary in their proximity to N_2O measurement sites.

Figure 10 shows the results for the same four locations shown in Fig. 8: KCMP tall tower (MN, USA), Hegyhátsál (Hungary), East China, and DR Congo. KCMP features continuous observations, and we see that emissions in this model grid cell can be constrained independently (averaging kernel value near 1.0, and near 0.0 elsewhere) from those in other places. Significant constraints are achieved at Hegyhátsál (averaging kernel value ~ 0.3), where weekly flask observations are available, though some spatial smearing is apparent. Weaker constraints (averaging kernel values up to ~ 0.03) are achieved in the vicinity of the East China grid box, likely provided by downwind observations in Korea and the western Pacific.

Averaging kernel values for the central African location are very low ($\sim 10^{-3}$), indicating little to no constraint on the source flux, and are also highly smeared spatially, showing that the current surface observations of N_2O do not allow emissions in that region to be independently resolved from emissions elsewhere across the globe. We see in Fig. 10 that this spatial smearing even extends to the midlatitudes in both hemispheres. Emissions in the under-constrained tropics thus risk being conflated with those in other, distant source regions in global inversion analyses.

The implications of this current lack of constraints on tropical N_2O emissions can be seen in a sample global inversion

based on real atmospheric data. Figure 11 shows a posteriori emission scaling factors for global inversions based on two different assumptions: the first uses our previous construction of the a priori error covariance matrix (100 % uncertainty with horizontal correlation length scales of 500 km over land and 1000 km over ocean); the other does not include any penalty term (measuring the departure from a priori conditions) in the cost function. When a priori constraints are included, the solution is relatively spatially smooth. To correct for a low bias in our a priori emissions inventory, emissions increase throughout those terrestrial and oceanic regions where emissions occur, with a slightly higher inferred flux over South America. Conversely, when we eliminate the a priori constraint, emissions increase strongly in the tropics and Southern Hemisphere, reaching a factor of 10 (the upper bound placed on the scaling factors) in South America near the beginning of the 2-year simulation. To compensate for this, the inferred emissions throughout the Northern Hemisphere decrease dramatically.

This severe sensitivity of the solution to the a priori error assumption reflects the ill-posed nature of the problem. It also highlights the fact that, because the global N_2O flux is constrained (as the N_2O lifetime and atmospheric burden are reasonably well-known), the lack of constraint on tropical emissions has important implications for understanding emissions elsewhere in the world.

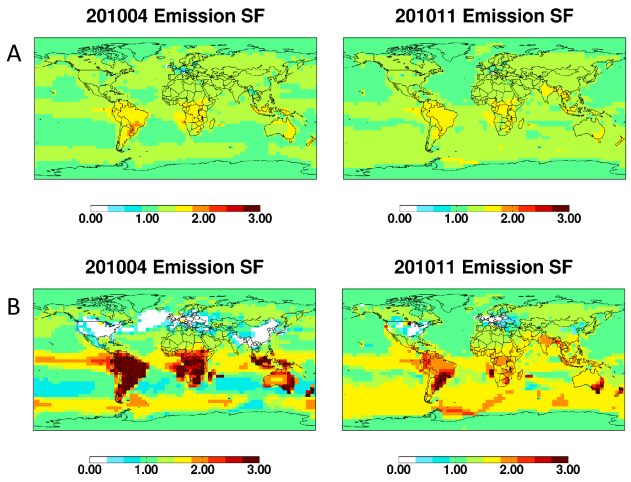

Figure 11. Inversion of N_2O emissions based on real surface observations. A posteriori emission scaling factors are shown for two different prior error assumptions: **(a)** 100 % a priori error and horizontal covariance length scales of 500 and 1000 km for land and ocean emissions, respectively; and **(b)** no penalty term in the cost function.

5.5 Identifying priority locations for future N_2O measurements

In this section, we apply the error reduction statistics derived above to identify priority regions where new observations are likely to have high value for improving present understanding of global N_2O sources. To that end, we carry out forward model simulations in which N_2O emissions in the first month are scaled by $(1-\boldsymbol{x})$, where $\boldsymbol{x}$ is the spatial map of relative error reductions achieved in the inversion on the basis of the surface observations (e.g., Fig. 9). The initial atmospheric burden of N_2O is set to zero, as are the emissions in subsequent months. The resulting atmospheric N_2O then reflects unconstrained emissions, and the distribution of that "unconstrained N_2O" in space and time shows where new observations are needed to quantify those emissions in a spatially explicit way.

Figure 12 shows the distribution of unconstrained N_2O mapped in the first and the second month following its emission. Results are shown for simulations starting in August 2010 and February 2011; these months were chosen to illustrate how seasonal differences in horizontal and vertical transport affect the atmospheric dispersion of unconstrained N_2O emissions. In August, unconstrained mixing ratios above 1 ppb can be found throughout Southeast Asia, central Africa, and South America, with the highest concentrations occurring over Brazil and off the western coasts of Africa and South America. Somewhat elevated concentrations (0.5–1 ppb) persist in these locations for the second month of the simulation, but these become well-dispersed in the following months (not shown). Unconstrained N_2O emitted in August is initially concentrated in the lower troposphere in the tropics and northern midlatitudes, but is lofted through the tropical troposphere by September. In contrast, unconstrained N_2O emitted in February is more strongly confined to the lower troposphere and the Northern Hemisphere, even a month after emission.

The maps in Fig. 12 rely by necessity on a particular a priori estimate of N_2O emissions and their distribution in space and time. However, they nonetheless provide an assessment of where additional measurements would have the best leverage for improving N_2O emission estimates, based on our existing bottom–up understanding of when and where those emissions occur. We see in the maps that areas over or downwind of the tropics and East Asia should receive the highest measurement priority to reduce uncertainty in the overall N_2O budget. As shown earlier, downwind surface observations can provide some spatially explicit emission constraints for regions with high fluxes; these may be the only feasible option for places where access, infrastructure, or political issues prevent sustained local measurements. We note that additional N_2O measurements are now available in and around Japan (Saikawa et al., 2014) that may provide additional constraints on East Asian emissions not achieved using the measurements presented here. In addition, aircraft measurements during the July–September time frame should have a strong value for constraining fluxes in the tropics, given the lofting and dispersal of those emissions that is apparent in the August 2010 simulation. The value of such measurements was

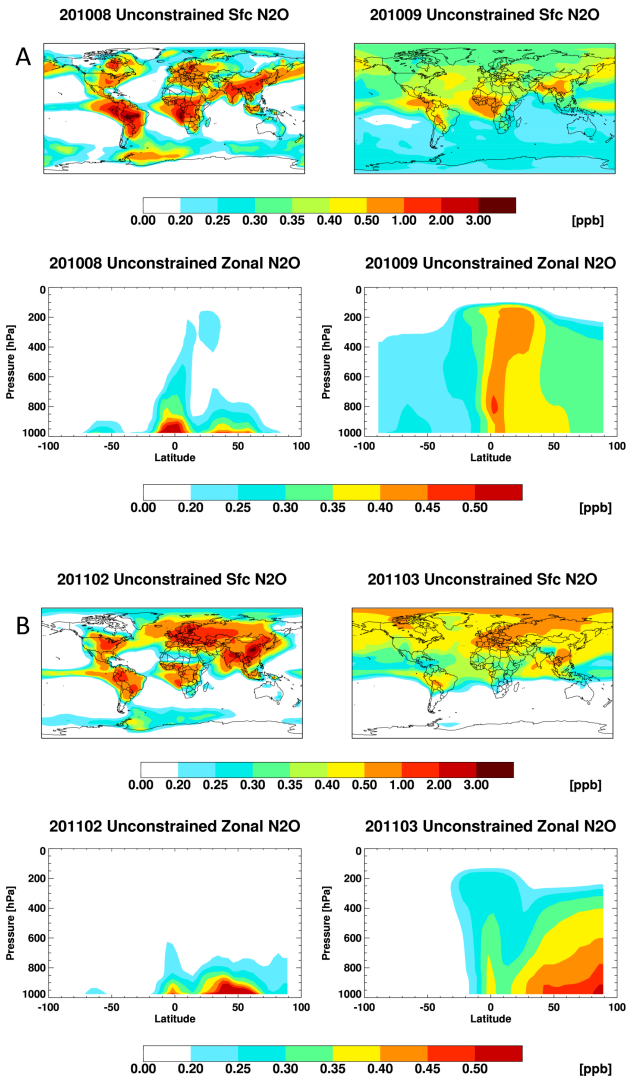

Figure 12. Distribution of unconstrained N_2O simulated by GEOS-Chem during the month of emission (**(a)** August 2010 and **(b)** February 2011) and the subsequent month. Unconstrained concentrations are calculated by scaling emissions for a particular month by $(1-\boldsymbol{x})$, where $\boldsymbol{x}$ is the map of emission error reductions achieved using surface observations of N_2O. The initial atmospheric burden of N_2O and the emissions in the ensuing months are set to zero in order to highlight the spatial dispersal of unconstrained N_2O. Note nonlinear color scales.

also pointed out by Kort et al. (2011), who reported observational evidence for lofting of large, episodic tropical emissions. On the other hand, Fig. 12 also reveals large areas of the world's oceans where additional surface measurements are not likely to provide appreciable new insights into the global N_2O budget, given the lack of unconstrained N_2O that is less than 1–2 months from emission.

6 Summary and conclusions

We developed a new inversion framework based on the GEOS-Chem model and its adjoint for estimating global N_2O emissions and stratospheric loss rates using surface (flask and in situ) as well as airborne (CARIBIC; HIPPO) measurements. We used this framework to (i) quantify the ability of the current observing network to constrain the global distribution of N_2O sources and sinks, (ii) assess the relative utility of the various observing platforms for doing so, and (iii) identify priority locations where measurements are most needed to improve the present understanding of the N_2O budget. Our simulation period runs from April 2010 to April 2012, with initial conditions constructed using surface flask observations and vertical profile measurements from the MLS satellite sensor.

Observing system simulation experiments (OSSEs) showed that the surface and HIPPO observations can accurately resolve a uniform bias in N_2O emissions for the first year of a 2-year simulation; in comparison, the sparser (and mostly high altitude) CARIBIC observations provide a weaker constraint. All three data sets are able to independently resolve the global surface flux to within 5 % of the truth. On the other hand, a seasonal emission bias is much more difficult to resolve given the long lifetime of N_2O, particularly in regions with sparse observations. The surface observations do provide a reduction of seasonal emission errors in the vicinity of measurement sites and in large source regions upwind.

The surface and airborne data sets are all able to resolve a global bias in the stratospheric loss rate of N_2O given known emissions, but do not give information on the spatial and temporal distribution of that sink. For the more realistic scenario with uncertain N_2O sources and sink, we find that resolving the two in a joint source–sink inversion would require greater confidence in modeled transport than is currently warranted. Nevertheless, because of the timescale for stratosphere–troposphere mixing, N_2O source inversions are insensitive to uncertainties in the chemical sink of N_2O on the 2 year analysis time frame used here (and assuming an accurate initial state; e.g., from interpolated data). However, a simple box model analysis shows that tropospheric N_2O is more sensitive to uncertainties in the rate of stratosphere–troposphere exchange (STE) than to those in the chemical loss rates for analysis timescales up to $\sim$ 3–4 years. Incomplete knowledge of STE rates will thus be a key source of uncertainty to address for N_2O source inversions on these timescales.

We employed a stochastic estimate of the inverse Hessian to quantify the spatial resolution of N_2O emission constraints afforded by the current global network of observations, and the degree to which emissions in a particular location can be distinguished from those elsewhere. Significant location-specific constraints are achieved in grid boxes near and immediately upwind of surface observation loca-

tions; however, these are mainly confined to North America, Europe and Australia. For sites with continuous surface observations, local emissions can be unambiguously resolved from those in surrounding locations, as indicated by large error reductions and averaging kernel (AK) values close to 1.0. Flask observations also provide significant local-to-regional constraints (e.g., AK values of ~ 0.3 at a site with weekly measurements). HIPPO observations primarily provide emission constraints for the Central US and East Asia. Critically, little to no spatial information on tropical emissions is provided by either set of observations: the corresponding AKs are highly smeared spatially and show that emissions in many parts of the tropics cannot even be resolved from those in the midlatitudes. For global inversions, this under-constraint in the tropics can thus lead to large errors in the inferred N_2O fluxes for the extratropics as well as the tropics themselves.

From the atmospheric distribution of "unconstrained N_2O" simulated based on the error reduction statistics achieved in the inversion and our a priori source estimates, we identify areas in the tropics and East Asia as the highest priorities for new N_2O measurements to advance understanding of the global budget. In situ or flask observations downwind of major sources in South America, central Africa, and East Asia can provide some spatial information on N_2O fluxes in cases where local, long-term measurements are impractical. Targeted aircraft measurements in the troposphere could also provide much-needed constraints on tropical emission fluxes, particularly during July–September when emissions are well-lofted vertically.

From our analysis it is clear that additional measurements are crucial to obtaining a more complete picture of global N_2O sources, particularly in the key areas mentioned above. In this context, we will further investigate the use of efficient randomization techniques to estimate the spatiotemporal constraints provided by new and existing N_2O measurements, and design optimal dimension approaches for N_2O source inversions. Such work could also include an evaluation of information provided by new N_2O retrievals from the Atmospheric Infrared Sounder (AIRS) (Xiong et al., 2014) and other space-based infrared sounders. While the vertical sensitivity of such instruments may be insufficient to derive useful direct information on surface emissions, such data could be useful for constraining the N_2O profile and its stratosphere–troposphere exchange (thus indirectly improving our ability to diagnose sources). The fact that the current observing system yields little information on the space–time distribution of N_2O fluxes over large parts of the world also speaks to the need for process-based emission models that can provide a priori source estimates that faithfully capture the key modes of variability. Such models are also needed to project how soil N_2O fluxes will respond to future changes in climate, hydrology, and nitrogen deposition and runoff.

Code availability

The N_2O version of the GEOS-Chem adjoint code is available via the GEOS-Chem adjoint repository. Instructions for obtaining access to the code can be found at http://wiki.seas.harvard.edu/geos-chem/index.php/GEOS-Chem_Adjoint.

The Supplement related to this article is available online at doi:10.5194/gmd-8-3179-2015-supplement.

Acknowledgements. This work was supported by NOAA (grant no. NA13OAR4310086) and the Minnesota Supercomputing Institute. We thank J. Muhle and C. Harth (UCSD-SIO), D. Young (U. Bristol), P. Fraser (CSIRO), R. Wang (GaTech), and other members of the AGAGE team for providing AGAGE data. The 6 AGAGE stations used here are supported principally by NASA (USA) grants to MIT and SIO, and also by DECC (UK) and NOAA (USA) grants to Bristol University, and by CSIRO and BoM (Australia). We thank Environment Canada for providing data from the Churchill, Estevan Point, East Trout Lake, Fraserdale, and Sable Island sites. We thank R. Martin and S. Nichol for providing data from the Arrival Heights NIWA station.

Edited by: O. Morgenstern

References

Assonov, S. S., Brenninkmeijer, C. A. M., Schuck, T., and Umezawa, T.: N_2O as a tracer of mixing stratospheric and tropospheric air based on CARIBIC data with applications for CO_2, Atmos. Environ., 79, 769–779, doi:10.1016/j.atmosenv.2013.07.035, 2013.

Bousserez, N., Henze, D. K., Perkins, A., Bowman, K. W., Lee, M., Liu, J., Deng, F., and Jones, D. B. A.: Improved analysis-error covariance matrix for high-dimensional variational inversions: application to source estimation using a 3D atmospheric transport model, Q. J. Roy. Meteor. Soc., 141, 1906–1921, doi:10.1002/qj.2495, 2015.

Bouwman, A. F.: Environmental science – Nitrogen oxides and tropical agriculture, Nature, 392, 866–867, doi:10.1038/31809, 1998.

Bouwman, A. F., Beusen, A. H. W., Griffioen, J., Van Groenigen, J. W., Hefting, M. M., Oenema, O., Van Puijenbroek, P. J. T. M., Seitzinger, S., Slomp, C. P., and Stehfest, E.: Global trends and uncertainties in terrestrial denitrification and N_2O emissions, Philos. T. R Soc. B, 368, 20130112, doi:10.1098/rstb.2013.0112, 2013.

Brenninkmeijer, C. A. M., Crutzen, P., Boumard, F., Dauer, T., Dix, B., Ebinghaus, R., Filippi, D., Fischer, H., Franke, H., Frieß, U., Heintzenberg, J., Helleis, F., Hermann, M., Kock, H. H., Koeppel, C., Lelieveld, J., Leuenberger, M., Martinsson, B. G., Miemczyk, S., Moret, H. P., Nguyen, H. N., Nyfeler, P., Oram, D., O'Sullivan, D., Penkett, S., Platt, U., Pupek, M., Ramonet, M., Randa, B., Reichelt, M., Rhee, T. S., Rohwer, J., Rosenfeld, K.,

Scharffe, D., Schlager, H., Schumann, U., Slemr, F., Sprung, D., Stock, P., Thaler, R., Valentino, F., van Velthoven, P., Waibel, A., Wandel, A., Waschitschek, K., Wiedensohler, A., Xueref-Remy, I., Zahn, A., Zech, U., and Ziereis, H.: Civil Aircraft for the regular investigation of the atmosphere based on an instrumented container: The new CARIBIC system, Atmos. Chem. Phys., 7, 4953–4976, doi:10.5194/acp-7-4953-2007, 2007.

Butterbach-Bahl, K., Baggs, E. M., Dannenmann, M., Kiese, R., and Zechmeister-Boltenstern, S.: Nitrous oxide emissions from soils: how well do we understand the processes and their controls?, Philos. T. R. Soc. B, 368, 20140122, doi:10.1098/rstb.2013.0122, 2013.

Byrd, R. H., Lu, P. H., Nocedal, J., and Zhu, C. Y.: A limited memory algorithm for bound constrained optimization, SIAM J. Sci. Comput., 16, 1190–1208, doi:10.1137/0916069, 1995.

Cohen, Y. and Gordon, L. I.: Nitrous oxide production in the ocean, J. Geophys. Res.-Oc. Atm., 84, 347–353, doi:10.1029/JC084iC01p00347, 1979.

Cooper, L. N., Steele, L. P., Langenfelds, R. L., Spencer, D. A., and Lucarelli, M. P.: Atmospheric methane, carbon dioxide, hydrogen, carbon monoxide and nitrous oxide from Cape Grim flask air samples analysed by gas chromatography, Baseline Atmospheric Program (Australia) 1996, 98–102, Bureau of Meteorology and CSIRO Atmospheric Research, 1999.

Davidson, E. A.: The contribution of manure and fertilizer nitrogen to atmospheric nitrous oxide since 1860, Nat. Geosci., 2, 659–662, doi:10.1038/ngeo608, 2009.

Deng, F., Jones, D. B. A., Walker, T. W., Keller, M., Bowman, K. W., Henze, D. K., Nassar, R., Kort, E. A., Wofsy, S. C., Walker, K. A., Bourassa, A. E., and Degenstein, D. A.: Sensitivity analysis of the potential impact of discrepancies in stratosphere–troposphere exchange on inferred sources and sinks of CO_2, Atmos. Chem. Phys. Discuss., 15, 10813–10851, doi:10.5194/acpd-15-10813-2015, 2015.

Denman, K. L., Brasseur, G. P., Chidthaisong, A., Ciais, P., Cox, P. M., Dickinson, R. E., Hauglustaine, D., Heinze, C., Holland, E., Jacob, D., Lohmann, U., Ramachandran, S., da Silva Dias, P. L., Wofsy, S. C., and Zhang, X.: Couplings Between Changes in the Climate System and Biogeochemistry, in: Climate Change 2007: Contribution of Working Group I to the Fourth Assessment Report of the Intergovernmental Panel on Climate Change, edited by: Solomon, S. D., Qin, D., Manning, M., Chen, Z., Marquis, M., Averyt, K. B., Tignor, M., and Miller, H. L., Cambridge University Press, Cambridge, 499–587, 2007.

Dlugokencky, E. J., Steele, L. P., Lang, P. M., and Masarie, K. A.: The growth rate and distrubution of atmospheric methane, J. Geophys. Res.-Atmos., 99, 17021–17043, doi:10.1029/94JD01245, 1994.

Elkins, J. W., Wofsy, S. C., McElroy, M. B., Kolb, C. E., and Kaplan, W. A.: Aquatic sources and sinks for nitrous oxide, Nature, 275, 602–606, 1978.

Firestone, M. K. and Davidson, E. A.: Microbiological basis of NO and N_2O production and consumption in the soil, in: Exchange of Trace Gases Between Terrestrial Ecosystems and the Atmosphere, edited by: Andreae, M. O., and Schimel, D. S., Wiley and Sons, Chichester, 7–21, 1989.

Forster, P., Ramaswamy, V., Artaxo, P., Berntsen, T., Betts, R., Fahey, D. W., Haywood, J., Lean, J., Lowe, D. C., Myrhe, G., Nganga, J., Prinn, R., Raga, G., Schulz, M., and Van Doorland, R.: Changes in atmospheric constituents and in radiative forcing, Cambridge, United Kingdom, and New York, NY, USA, 2007.

Francey, R. J., Steele, L. P., Langenfelds, R. L., Lucarelli, M. P., Allison, C. E., Beardsmore, D. J., Coram, S. A., Derek, N., de Silva, F. R., Etheridge, D. M., Fraser, P. J., Henry, R. J., Turner, B., Welch, E. D., Spencer, D. A., and Cooper, L. N.: Global Atmospheric Sampling Laboratory (GASLAB): supporting and extending the Cape Grim trace gas programs, Baseline Atmospheric Program (Australia) 1993, 8–29, Bureau of Meteorology and CSIRO division of Atmospheric Research, 1996.

Galloway, J. N., Townsend, A. R., Erisman, J. W., Bekunda, M., Cai, Z. C., Freney, J. R., Martinelli, L. A., Seitzinger, S. P., and Sutton, M. A.: Transformation of the nitrogen cycle: Recent trends, questions, and potential solutions, Science, 320, 889–892, doi:10.1126/science.1136674, 2008.

Griffis, T. J., Lee, X., Baker, J. M., Russelle, M. P., Zhang, X., Venterea, R., and Millet, D. B.: Reconciling the differences between top-down and bottom-up estimates of nitrous oxide emissions for the US Corn Belt, Global Biogeochem. Cy., 27, 746–754, doi:10.1002/gbc.20066, 2013.

Henze, D. K., Hakami, A., and Seinfeld, J. H.: Development of the adjoint of GEOS-Chem, Atmos. Chem. Phys., 7, 2413–2433, doi:10.5194/acp-7-2413-2007, 2007.

Henze, D. K., Seinfeld, J. H., and Shindell, D. T.: Inverse modeling and mapping US air quality influences of inorganic $PM_{2.5}$ precursor emissions using the adjoint of GEOS-Chem, Atmos. Chem. Phys., 9, 5877–5903, doi:10.5194/acp-9-5877-2009, 2009.

Hirsch, A. I., Michalak, A. M., Bruhwiler, L. M., Peters, W., Dlugokencky, E. J., and Tans, P. P.: Inverse modeling estimates of the global nitrous oxide surface flux from 1998–2001, Global Biogeochem. Cy., 20, GB1008, doi:10.1029/2004gb002443, 2006.

Huang, J., Golombek, A., Prinn, R., Weiss, R., Fraser, P., Simmonds, P., Dlugokencky, E. J., Hall, B., Elkins, J., Steele, P., Langenfelds, R., Krummel, P., Dutton, G., and Porter, L.: Estimation of regional emissions of nitrous oxide from 1997 to 2005 using multinetwork measurements, a chemical transport model, and an inverse method, J. Geophys. Res., 113, D17313, doi:10.1029/2007JD009381, 2008.

IPCC: 2006 IPCC Guidelines for National Greenhouse Gas Inventories, Prepared by the National Greenhouse Gas Inventories Programme, edited by: Eggleston, H. S., Buendia, L., Miwa, K., Ngara, T., and Tanabe, K., IGES, Japan, 2006.

Jiang, Z., Jones, D. B. A., Kopacz, M., Liu, J., Henze, D. K., and Heald, C.: Quantifying the impact of model errors on top-down estimates of carbon monoxide emissions using satellite observations, J. Geophys. Res.-Atmos, 116, D15306, doi:10.1029/2010JD015282, 2011.

Jiang, Z., Jones, D. B. A., Worden, H. M., Deeter, M. N., Henze, D. K., Worden, J., Bowman, K. W., Brenninkmeijer, C. A. M., and Schuck, T. J.: Impact of model errors in convective transport on CO source estimates inferred from MOPITT CO retrievals, J. Geophys. Res., 118, 2073–2083, doi:10.1002/jgrd.50216, 2013.

Jin, X. and Gruber, N.: Offsetting the radiative benefit of ocean iron fertilization by enhancing N_2O emissions, Geophys. Res. Lett., 30, 2249, doi:10.1029/2003GL018458, 2003.

Kopacz, M., Jacob, D. J., Henze, D. K., Heald, C. L., Streets, D. G., and Zhang, Q.: Comparison of adjoint and analytical Bayesian inversion methods for constraining Asian sources

of carbon monoxide using satellite (MOPITT) measurements of CO columns, J. Geophys. Res.-Atmos., 114, D04305, doi:10.1029/2007JD009264, 2009.

Kopacz, M., Jacob, D. J., Fisher, J. A., Logan, J. A., Zhang, L., Megretskaia, I. A., Yantosca, R. M., Singh, K., Henze, D. K., Burrows, J. P., Buchwitz, M., Khlystova, I., McMillan, W. W., Gille, J. C., Edwards, D. P., Eldering, A., Thouret, V., and Nedelec, P.: Global estimates of CO sources with high resolution by adjoint inversion of multiple satellite datasets (MOPITT, AIRS, SCIAMACHY, TES), Atmos. Chem. Phys., 10, 855–876, doi:10.5194/acp-10-855-2010, 2010.

Kopacz, M., Mauzerall, D. L., Wang, J., Leibensperger, E. M., Henze, D. K., and Singh, K.: Origin and radiative forcing of black carbon transported to the Himalayas and Tibetan Plateau, Atmos. Chem. Phys., 11, 2837–2852, doi:10.5194/acp-11-2837-2011, 2011.

Kort, E. A., Patra, P. K., Ishijima, K., Daube, B. C., Jimenez, R., Elkins, J., Hurst, D., Moore, F. L., Sweeney, C., Wofsy, S. C.: Tropospheric distribution and variability of N_2O: Evidence for strong tropical emissions, Geophys. Res. Lett., 38, L15806, doi:10.1029/2011GL047612, 2011.

Lambert, A., Read, W. G., Livesey, N. J., Santee, M. L., Manney, G. L., Froidevaux, L., Wu, D. L., Schwartz, M. J., Pumphrey, H. C., Jimenez, C., Nedoluha, G. E., Cofield, R. E., Cuddy, D. T., Daffer, W. H., Drouin, B. J., Fuller, R. A., Jarnot, R. F., Knosp, B. W., Pickett, H. M., Perun, V. S., Snyder, W. V., Stek, P. C., Thurstans, R. P., Wagner, P. A., Waters, J. W., Jucks, K. W., Toon, G. C., Stachnik, R. A., Bernath, P. F., Boone, C. D., Walker, K. A., Urban, J., Murtagh, D., Elkins, J. W., and Atlas, E.: Validation of the Aura Microwave Limb Sounder middle atmosphere water vapor and nitrous oxide measurements, J. Geophys. Res.-Atmos., 112, D24S36, doi:10.1029/2007JD008724, 2007.

Law, C. S. and Owens, N. J. P.: Significant flux of atmospheric nitrous oxide from the northwest Indian Ocean, Nature, 346, 826–828, doi:10.1038/346826a0, 1990.

Maggiotto, S. R., Webb, J. A., Wagner-Riddle, C., and Thurtell, G. W.: Nitrous and nitrogen oxide emissions from turfgrass receiving different forms of nitrogen fertilizer, J. Environ. Qual., 29, 621–630, 2000.

Miller, S. M., Kort, E. A., Hirsch, A. I., Dlugokencky, E. J., Andrews, A. E., Xu, X., Tian, H., Nehrkorn, T., Eluszkiewicz, J., Michalak, A. M., and Wofsy, S. C.: Regional sources of nitrous oxide over the United States: Seasonal variation and spatial distribution, J. Geophys. Res.-Atmos., 117, D06310, doi:10.1029/2011JD016951, 2012.

Mosier, A., Kroeze, C., Nevison, C., Oenema, O., Seitzinger, S., and van Cleemput, O.: Closing the global N_2O budget: nitrous oxide emissions through the agricultural nitrogen cycle – OECD/IPCC/IEA phase II development of IPCC guidelines for national greenhouse gas inventory methodology, Nutr. Cycl. Agroecosys., 52, 225–248, doi:10.1023/a:1009740530221, 1998.

Nevison, C. D., Keeling, R. F., Weiss, R. F., Popp, B. N., Jin, X., Fraser, P. J., Porter, L. W., and Hess, P. G.: Southern Ocean ventilation inferred from seasonal cycles of atmospheric N_2O and O_2/N_2 at Cape Grim, Tasmania, Tellus B, 57, 218–229, doi:10.1111/j.1600-0889.2005.00143.x, 2005.

Nevison, C. D., Dlugokencky, E., Dutton, G., Elkins, J. W., Fraser, P., Hall, B., Krummel, P. B., Langenfelds, R. L., O'Doherty, S., Prinn, R. G., Steele, L. P., and Weiss, R. F.: Exploring causes of interannual variability in the seasonal cycles of tropospheric nitrous oxide, Atmos. Chem. Phys., 11, 3713–3730, doi:10.5194/acp-11-3713-2011, 2011.

Park, S., Croteau, P., Boering, K. A., Etheridge, D. M., Ferretti, D., Fraser, P. J., Kim, K. R., Krummel, P. B., Langenfelds, R. L., van Ommen, T. D., Steele, L. P., and Trudinger, C. M.: Trends and seasonal cycles in the isotopic composition of nitrous oxide since 1940, Nat. Geosci., 5, 261–265, doi:10.1038/ngeo1421, 2012.

Parrington, M., Palmer, P. I., Henze, D. K., Tarasick, D. W., Hyer, E. J., Owen, R. C., Helmig, D., Clerbaux, C., Bowman, K. W., Deeter, M. N., Barratt, E. M., Coheur, P.-F., Hurtmans, D., Jiang, Z., George, M., and Worden, J. R.: The influence of boreal biomass burning emissions on the distribution of tropospheric ozone over North America and the North Atlantic during 2010, Atmos. Chem. Phys., 12, 2077–2098, doi:10.5194/acp-12-2077-2012, 2012.

Potter, C. S., Matson, P. A., Vitousek, P. M., and Davidson, E. A.: Process modeling of controls on nitrogen trace gas emissions from soils worldwide, J. Geophys. Res.-Atmos., 101, 1361–1377, doi:10.1029/95JD02028, 1996.

Prather, M. J., Holmes, C. D., and Hsu, J.: Reactive greenhouse gas scenarios: Systematic exploration of uncertainties and the role of atmospheric chemistry, Geophys. Res. Lett., 39, L09803, doi:10.1029/2012GL051440, 2012.

Prinn, R. G., Weiss, R. F., Fraser, P. J., Simmonds, P. G., Cunnold, D. M., Alyea, F. N., O'Doherty, S., Salameh, P., Miller, B. R., Huang, J., Wang, R. H. J., Hartley, D. E., Harth, C., Steele, L. P., Sturrock, G., Midgley, P. M., and McCulloch, A.: A history of chemically and radiatively important gases in air deduced from ALE/GAGE/AGAGE, J. Geophys. Res., 105, 17751–17792, doi:10.1029/2000JD900141, 2000.

Rauthe-Schöch, A., Weigelt, A., Hermann, M., Martinsson, B. G., Baker, A. K., Heue, K.-P., Brenninkmeijer, C. A. M., Zahn, A., Scharffe, D., Eckhardt, S., Stohl, A., and van Velthoven, P. F. J.: CARIBIC aircraft measurements of Eyjafjallajökull volcanic clouds in April/May 2010, Atmos. Chem. Phys., 12, 879–902, doi:10.5194/acp-12-879-2012, 2012.

Ravishankara, A. R., Daniel, J. S., and Portmann, R. W.: Nitrous Oxide (N_2O): The Dominant Ozone-Depleting Substance Emitted in the 21st Century, Science, 326, 123–125, doi:10.1126/science.1176985, 2009.

Saikawa, E., Prinn, R. G., Dlugokencky, E., Ishijima, K., Dutton, G. S., Hall, B. D., Langenfelds, R., Tohjima, Y., Machida, T., Manizza, M., Rigby, M., O'Doherty, S., Patra, P. K., Harth, C. M., Weiss, R. F., Krummel, P. B., van der Schoot, M., Fraser, P. J., Steele, L. P., Aoki, S., Nakazawa, T., and Elkins, J. W.: Global and regional emissions estimates for N_2O, Atmos. Chem. Phys., 14, 4617–4641, doi:10.5194/acp-14-4617-2014, 2014.

Salstein, D. A.: Mean properties of the atmosphere, in: Composition, Chemistry, and Climate of the Atmosphere, edited by: Singh, H. B., Van Nostrand Reinhold, New York, 19–49, 1995.

Schuck, T. J., Brenninkmeijer, C. A. M., Slemr, F., Xueref-Remy, I., and Zahn, A.: Greenhouse gas analysis of air samples collected onboard the CARIBIC passenger aircraft, Atmos. Meas. Tech., 2, 449–464, doi:10.5194/amt-2-449-2009, 2009.

Shcherbak, I., Millar, N., and Robertson, G. P.: Global metaanalysis of the nonlinear response of soil nitrous oxide (N_2O) emissions

to fertilizer nitrogen, P. Natl. Acad. Sci. USA, 111, 9199–9204, doi:10.1073/pnas.1322434111, 2014.

Thompson, R. L., Bousquet, P., Chevallier, F., Rayner, P. J., and Ciais, P.: Impact of the atmospheric sink and vertical mixing on nitrous oxide fluxes estimated using inversion methods, J. Geophys. Res.-Atmos., 116, D17307, doi:10.1029/2011JD015815, 2011.

Thompson, R. L., Chevallier, F., Crotwell, A. M., Dutton, G., Langenfelds, R. L., Prinn, R. G., Weiss, R. F., Tohjima, Y., Nakazawa, T., Krummel, P. B., Steele, L. P., Fraser, P., O'Doherty, S., Ishijima, K., and Aoki, S.: Nitrous oxide emissions 1999 to 2009 from a global atmospheric inversion, Atmos. Chem. Phys., 14, 1801–1817, doi:10.5194/acp-14-1801-2014, 2014a.

Thompson, R. L., Patra, P. K., Ishijima, K., Saikawa, E., Corazza, M., Karstens, U., Wilson, C., Bergamaschi, P., Dlugokencky, E., Sweeney, C., Prinn, R. G., Weiss, R. F., O'Doherty, S., Fraser, P. J., Steele, L. P., Krummel, P. B., Saunois, M., Chipperfield, M., and Bousquet, P.: TransCom N_2O model inter-comparison – Part 1: Assessing the influence of transport and surface fluxes on tropospheric N_2O variability, Atmos. Chem. Phys., 14, 4349–4368, doi:10.5194/acp-14-4349-2014, 2014b.

Thompson, R. L., Ishijima, K., Saikawa, E., Corazza, M., Karstens, U., Patra, P. K., Bergamaschi, P., Chevallier, F., Dlugokencky, E., Prinn, R. G., Weiss, R. F., O'Doherty, S., Fraser, P. J., Steele, L. P., Krummel, P. B., Vermeulen, A., Tohjima, Y., Jordan, A., Haszpra, L., Steinbacher, M., Van der Laan, S., Aalto, T., Meinhardt, F., Popa, M. E., Moncrieff, J., and Bousquet, P.: TransCom N_2O model inter-comparison – Part 2: Atmospheric inversion estimates of N_2O emissions, Atmos. Chem. Phys., 14, 6177–6194, doi:10.5194/acp-14-6177-2014, 2014c.

Umezawa, T., Baker, A. K., Oram, D., Sauvage, C., O'Sullivan, D., Rauthe-Schoch, A., Montzka, S. A., Zahn, A., and Brenninkmeijer, C. A. M.: Methyl chloride in the upper troposphere observed by CARIBIC passenger aircraft observatory: Large-scale distributions and Asian summer monsoon outflow, J. Geophys. Res.-Atmos., 119, 5542–5558, doi:10.1002/2013JD021396, 2014.

van der Werf, G. R., Randerson, J. T., Giglio, L., Collatz, G. J., Mu, M., Kasibhatla, P. S., Morton, D. C., DeFries, R. S., Jin, Y., and van Leeuwen, T. T.: Global fire emissions and the contribution of deforestation, savanna, forest, agricultural, and peat fires (1997–2009), Atmos. Chem. Phys., 10, 11707–11735, doi:10.5194/acp-10-11707-2010, 2010.

Volk, C. M., Elkins, J. W., Fahey, D. W., Dutton, G. S., Gilligan, J. M., Loewenstein, M., Podolske, J. R., Chan, K. R., and Gunson, M. R.: Evaluation of source gas lifetimes from stratospheric observations, J. Geophys. Res.-Atmos., 102, 25543–25564, doi:10.1029/97JD02215, 1997.

Wagner-Riddle, C., Furon, A., McLaughlin, N. L., Lee, I., Barbeau, J., Jayasundara, S., Parkin, G., Von Bertoldi, P., and Warland, J.: Intensive measurement of nitrous oxide emissions from a corn-soybean-wheat rotation under two contrasting management systems over 5 years, Glob. Change Biol., 13, 1722–1736, doi:10.1111/j.1365-2486.2007.01388.x, 2007.

Wang, J., Xu, X., Henze, D. K., Zeng, J., Ji, Q., Tsay, S.-C., and Huang, J.: Top-down estimate of dust emissions through integration of MODIS and MISR aerosol retrievals with the GEOS-Chem adjoint model, Geophys. Res. Lett., 39, L08802, doi:10.1029/2012GL051136, 2012.

Wells, K. C., Millet, D. B., Cady-Pereira, K. E., Shephard, M. W., Henze, D. K., Bousserez, N., Apel, E. C., de Gouw, J., Warneke, C., and Singh, H. B.: Quantifying global terrestrial methanol emissions using observations from the TES satellite sensor, Atmos. Chem. Phys., 14, 2555–2570, doi:10.5194/acp-14-2555-2014, 2014.

Wofsy, S. C.: HIAPER Pole-to-Pole Observations (HIPPO): fine-grained, global-scale measurements of climatically important atmospheric gases and aerosols, Philos. T. R. Soc. A, 369, 2073–2086, doi:10.1098/rsta.2010.0313, 2011.

Xiong, X., Maddy, E. S., Barnet, C., Gambacorta, A., Patra, P. K., Sun, F., and Goldberg, M.: Retrieval of nitrous oxide from Atmospheric Infrared Sounder: Characterization and validation, J. Geophys. Res.-Atmos., 119, 9107–9122, doi:10.1002/2013JD021406, 2014.

Xu, X., Wang, J., Henze, D. K., Qu, W., and Kopacz, M.: Constraints on aerosol sources using GEOS-Chem adjoint and MODIS radiances, and evaluation with multisensor (OMI, MISR) data, J. Geophys. Res.-Atmos., 118, 6396–6413, doi:10.1002/jgrd.50515, 2013.

Zhang, L., Jacob, D. J., Kopacz, M., Henze, D. K., Singh, K., and Jaffe, D. A.: Intercontinental source attribution of ozone pollution at western US sites using an adjoint method, Geophys. Res. Lett., 36, L11810, doi:10.1029/2009GL037950, 2009.

Zhu, C., Byrd, R. H., Lu, P., and Nocedal, J.: L-BFGS-B: a limited memory FORTRAN code for solving bound constrained optimization problems, Tech. rep., Northwestern University, Evanston, Illinois, 1994.

Zhu, L., Henze, D. K., Cady-Pereira, K. E., Shephard, M. W., Luo, M., Pinder, R. W., Bash, J. O., and Jeong, G. R.: Constraining U.S. ammonia emissions using TES remote sensing observations and the GEOS-Chem adjoint model, J. Geophys. Res.-Atmos, 118, 3355–3368, doi:10.1002/jgrd.50166, 2013.